Geochemistry Geophysics Geosystems G3
AN ELECTRONIC JOURNAL OF THE EARTH SCIENCES
Published by AGU and the Geochemical Society

Article
Volume 7, Number 5
3 May 2006
Q05002, doi:10.1029/2005GC001011
ISSN: 1525-2027

Hydrothermal mineral deposits and fossil biota from a young (0.1 Ma) abyssal hill on the flank of the fast spreading East Pacific Rise: Evidence for pulsed hydrothermal flow and tectonic tapping of axial heat and fluids

Sara B. Benjamin and Rachel M. Haymon

Department of Earth Science and Marine Science Institute, University of California, Santa Barbara, California 93106, USA (haymon@geol.ucsb.edu)

[1] Heat flow data indicate that most hydrothermal heat loss from ocean lithosphere occurs on the flanks of the mid-ocean ridge, but few ridge flank hydrothermal sites are known. We describe the first nonseamount, abyssal hill hydrothermal mineral deposits to be recovered from the fast spreading East Pacific Rise (EPR) flanks. Deposits were sampled at two sites on an abyssal hill ~5 km east of the EPR axis, just north of Clipperton Fracture Zone at 10°20′N, on ~0.1 Ma lithosphere. "Tevnia Site" is on the axis-facing fault scarp of the hill, and "Ochre Site" is located ~950 m farther east near the base of the outward-facing slope. Clusters of fragile, biodegradable *Tevnia* worm tubes at both sites indicate that hydrothermal fluids carried sufficient H_2S to sustain *Tevnia* worms, and that fluid flow waned too recently to allow time for tube destruction. Presence of microbial mats and other biota also are consistent with recent waning of flow. The deposits are mineralogically zoned, from nontronite-celadonite to hydrous Fe-oxide+opaline silica to Mn-oxide (birnessite and todorokite). This places them into a distinctive class of Fe-Si-Mn hydrothermal deposits found along tectonic cracks and faults in young oceanic crust, and suggests that (1) deposits precipitated along an O_2 gradient between ambient seawater and hydrothermal fluid; (2) fluid temperatures were <150°C; and (3) undiluted fluids were Mg-depleted, and Fe-, K-, Si- and Mn-enriched. These fluids may derive from high temperature seawater-basalt interaction ± phase separation proximal to the axial melt zone, and lose Cu and Zn before venting due to conductive cooling and/or pH increase. Ochre Site samples are purely hydrothermal; however, Tevnia Site samples incorporate volcanic, sedimentary, and fossil components, and exhibit at least three generations of fracturing and hydrothermal cementation. The Tevnia Site breccias accumulated on the exposed fault scarp, possibly during multiple slip events and hydrothermal pulses as the abyssal hill was uplifted. We hypothesize that frequent earthquakes rejuvenate young abyssal hill hydrothermal systems episodically over 10^4–10^5 years, tapping axial heat and hydrothermal fluids, sustaining biota, and likely helping to chill the margins of the axial melt zone.

Components: 15,443 words, 15 figures, 6 tables.

Keywords: equatorial Pacific; excursion; orbital modulation; paleointensity; paleomagnetism.

Index Terms: 3017 Marine Geology and Geophysics: Hydrothermal systems (0450, 1034, 3616, 4832, 8135, 8424); 3021 Marine Geology and Geophysics: Marine hydrogeology; 3035 Marine Geology and Geophysics: Midocean ridge processes.

Received 7 May 2005; **Revised** 27 September 2005; **Accepted** 15 December 2005; **Published** 3 May 2006.

Benjamin, S. B., and R. M. Haymon (2006), Hydrothermal mineral deposits and fossil biota from a young (0.1 Ma) abyssal hill on the flank of the fast spreading East Pacific Rise: Evidence for pulsed hydrothermal flow and tectonic tapping of axial heat and fluids, *Geochem. Geophys. Geosyst.*, *7*, Q05002, doi:10.1029/2005GC001011.

1. Introduction

[2] Heat flow measured in ocean lithosphere younger than ~65 Ma is below model predictions of heat flow from a conductively cooled plate. This is attributed to hydrothermal cooling of the lithosphere on the crest and flanks of the mid-ocean ridge [*Williams et al.*, 1974; *Anderson et al.*, 1977; *Stein et al.*, 1995]. From a synthesis of global heat flow data, it is estimated that heat flux of $\sim 11 \pm 4 \times 10^{12}$ W is removed from ocean lithosphere by hydrothermal advection, and that a large majority (up to 70–90%) of this hydrothermal heat flux occurs on ridge flanks in seafloor ≥100,000 years old [*Johnson and Pruis*, 2003; *Stein and Stein*, 1994; *Morton and Sleep*, 1985].

[3] It is notable that fully half of the ridge-flank hydrothermal heat loss occurs during the first 5 Ma in thinly sedimented abyssal hill terrain on mid-ocean ridge flanks [*Johnson and Pruis*, 2003]. Supporting evidence for large magnitude hydrothermal flux from young abyssal hills includes progressive rapid increase in seismic velocity of Layer 2A in 0–5 Ma crust on the East Pacific Rise (EPR) flank [*Carlson*, 1998] and concomitant decrease in crustal porosity [*Fisher and Becker*, 2000], which are both attributable to the filling of voids by minerals precipitated from freely circulating hydrothermal fluids. Added evidence is the extensive alteration and veining [*Alt*, 1995] observed in 6.9 Ma (D. Wilson, personal communication, 2005) drill core from the Nazca plate at Hole 504b. The role of young abyssal hills in ridge flank hydrothermal cooling may be particularly important at fast and intermediate spreading rates. On the intermediate-rate Juan de Fuca Ridge, *Kappel and Ryan* [1986] proposed that abyssal hills form from tectonic splitting of elongate axial volcanic ridges constructed at the ridge axis. Studies of EPR abyssal hills show that the overwhelming majority of these hills are not split axial volcanic ridges, but instead have formed from volcanic growth faults that begin to develop within a few kilometers of the ridge axis [*Macdonald et al.*, 1996]. On the EPR flanks, hills are rapidly uplifted as much as 250 m in 100,000–700,000 years, at distances of 5–40 km away from the ridge axis [*Alexander and Macdonald*, 1996; *Crowder and Macdonald*, 2000].

[4] Despite the large magnitude of estimated ridge flank hydrothermal heat loss, and its possible chemical and biological consequences, very little is known about characteristics of hydrothermal vents and mineral deposits in the abyssal hill-dominated terrain covering vast areas of the ocean floor [*Macdonald et al.*, 1996]. Most prior work on ridge flank hydrothermal activity has focused on venting associated with ridge flank volcanic seamounts [e.g., *Alt et al.*, 1985; *Hekinian and Fouquet*, 1985; *Mottl et al.*, 1998; *Fisher et al.*, 2003a, 2003b]. Only two previously reported ridge flank hydrothermal sites are clearly unrelated to seamounts: the Galapagos Mounds on 0.6 Ma seafloor south of the Galapagos Rift [*Lonsdale*, 1977; *Williams et al.*, 1979; *Honnorez et al.*, 1983], and Lost City, on 1 Ma seafloor west of the Mid-Atlantic Ridge (MAR) [*Kelley et al.*, 2001]. Our study of EPR abyssal hill hydrothermal samples is the first description of non-seamount hydrothermal deposits on the flanks of a fast spreading ridge, and is the youngest example of nonseamount ridge flank deposits yet documented.

2. Site Descriptions

[5] Samples of hydrothermal mineral deposits were collected on the EPR flank with the *Alvin* submersible on Dive 2695 in January of 1994. The samples were recovered from a fault-bounded abyssal hill, located ~5–6 km east of the EPR axis and just north of the Clipperton Fracture Zone (Figure 1). On the basis of a full spreading rate of 109 mm/y for the EPR in this area [*Carbotte and Macdonald*, 1992], the deposits are located on crust that is ~100,000 years old (0.1 Ma).

[6] A total of three samples were recovered from two recently active hydrothermal sites: "Tevnia Site" and "Ochre Site." Samples 2695-1 and 2695-2 were both collected from Tevnia Site, situated on the essentially vertical, axis-facing fault scarp bounding the west side of the abyssal hill, at 10°20′N, 103°33.2′W and 2900 m depth (Figure 1). Sample 2695-4 was collected from Ochre Site at the base of the east slope of the hill (10°20′N, 103°32.6′W, 2966 m depth; Figure 1), where the outward-facing fault scarp is draped by lobate lava flows [*Macdonald et al.*, 1996].

[7] Traversing the abyssal hill from west to east (Figures 1b and 1c), *Alvin* divers encountered well-sorted, fresh-looking talus cut by a series of meter-wide, ridge-parallel fissures on the western side, and then ascended the nearly vertical, axis-facing scarp in which freshly truncated layer 2A volcanic flows are exposed. Tevnia Site was discovered halfway up this steep western fault scarp where

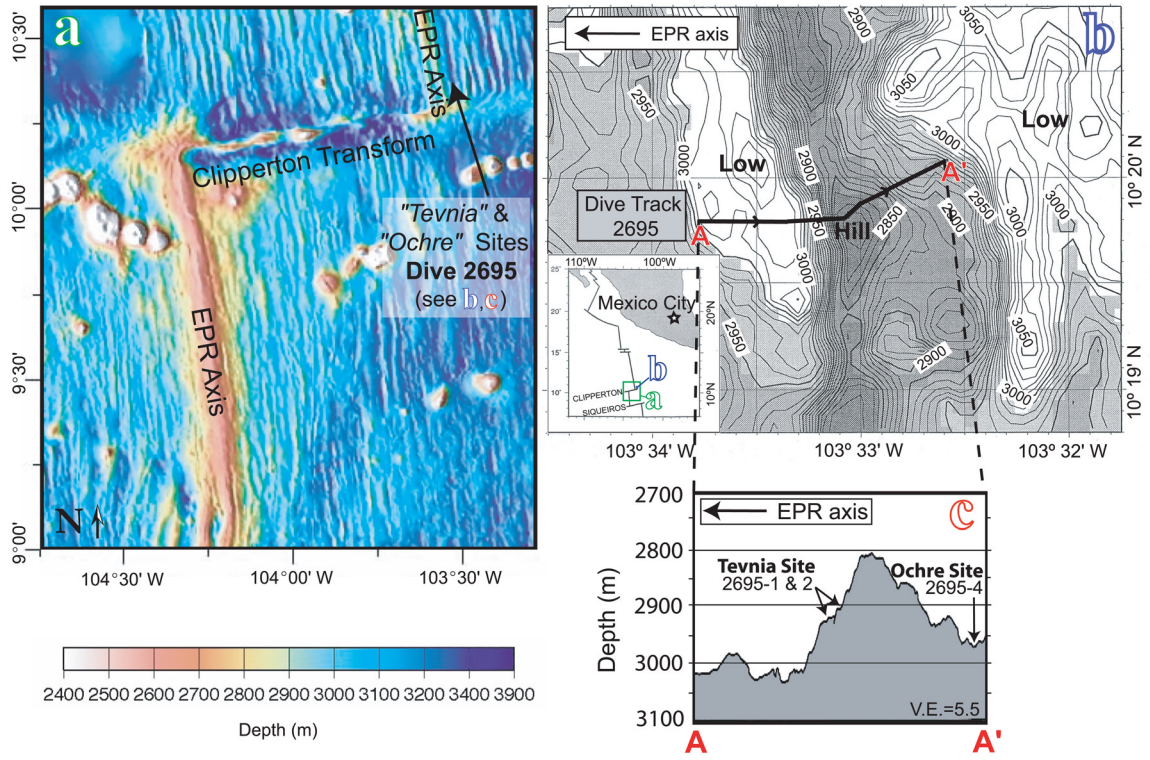

Figure 1. (a) Regional color shaded relief bathymetric map of the East Pacific Rise, 9°–11°N; arrow points to the site of the young abyssal hill where Tevnia and Ochre Sites are located. (b) Multibeam bathymetric map of dive site, located north of the Clipperton Fracture Zone and ~5–6 km east of the EPR axis; geographic location of map area shown by inset map at lower left and in Figure 1a. Dive track of *Alvin* Dive 2695 across abyssal hill is shown from A to A′; arrowheads indicate direction of travel along traverse. Contour intervals = 50 m; higher elevations are shaded. (c) *Alvin* depth profile across the young abyssal hill from A to A′. Labeled arrows show locations of collected hydrothermal samples. Dead colonies of *Tevnia* tube worms were observed at both sites (see Figure 2).

discrete colonies of intact dead *Tevnia* worm tubes were observed clinging to the scarp (Figure 2). Divers identified these tubes as *Tevnia* because they observed the characteristic closely spaced concentric ridges created by flanges on the tubes of this species (K. Macdonald, personal communication, 2005). Each clump of *Tevnia* tubes was encircled by a halo of ochre-yellow staining on the surrounding substrate. Samples 2695-1 and 2695-2 (Figures 1c and 3) were collected at depths of 2924 m and 2911 m (respectively) from dark-colored, concretionary material locally covering the fault surface near the yellow-stained *Tevnia* tubes (Figure 2). *Tevnia* is an early-colonizing species of tubeworm that is common at active hydrothermal sites on the EPR crest [*Shank et al.*, 1998]. Because *Tevnia* require reduced sulfur compounds, their occurrence here demonstrates that reduced hydrothermal fluids were emitted from the scarp at the time of colonization. Preservation of fragile *Tevnia* worm tubes, which are subject to biological and mechanical degradation (including events of mass wasting along the active fault scarp), suggests relatively recent hydrothermal activity. Galatheid crabs, shrimp (Figures 4b and 4c), "dandelion" siphonophores, and mossy microbial floc attached to the fault scarp face were reported and/or photographed by divers at Tevnia Site. These organisms typically inhabit active diffuse flow vent sites on the EPR axis [*Shank et al.*, 1998]. Their presence suggests that fluid discharge here was either ongoing and invisibly diffuse or had ceased only recently (i.e., within months) prior to Dive 2695. No temperature anomalies could be measured at the site because the *Alvin* low-T probe was not functioning during Dive 2695 (K. Macdonald, personal communication, 2005).

[8] After sampling Tevnia Site, the submersible drove to the top of the scarp, where sediment cover is ~10–20 cm thick and forms pockets between pillows. *Alvin* crossed the crest of the abyssal ridge at ~2800 m, and continued down the east side of the hill (see Figure 1). The lava-draped eastern

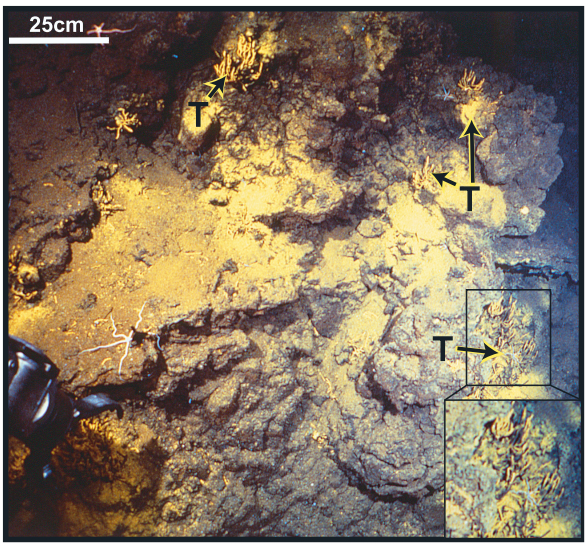

Figure 2. *Alvin* 35-mm film photograph of Tevnia Site, taken at ~2900 m depth on the western fault scarp of the abyssal hill during *Alvin* Dive 2695; arrows point to clumps of *Tevnia* worm tubes ("T"); inset photo shows close-up of worm tubes; yellow-orange patches on scarp are hydrothermal mineral deposits (Figure 3); *Alvin* heading ~110 (ESE).

slope of the hill, unlike the steeper west-facing scarp, is dominated by volcanic flows and constructional features. Both elongate and bulbous pillows were observed near the base of the eastern slope. At a depth of ~2970 m, *Alvin* encountered a second hydrothermal area which we have named "Ochre Site." Like Tevnia Site, the seafloor at Ochre Site is covered by a pavement of mineral encrustation with a rough-textured, dark-colored upper surface that is accented by discrete patches of bright yellow *Tevnia* clumps. At the jagged edges of the encrustation, yellow mineralization is visible underneath the dark-colored upper crust (Figure 5). Sample 2695-4 (Figure 6) was collected from this concretionary material at a depth of 2966 m (see Figure 1c). The dark-colored surficial material in the seafloor photos (Figure 5) corresponds to Layer III in the sample photo (Figure 6), and the yellow mineralization in the seafloor photos corresponds to Layer II.

3. Methods of Sample Documentation and Analysis

[9] Prior to analysis, the hydrothermal samples were photo-documented and visually described. To identify the mineral phases present, three standard analytical methods were used: reflected/transmitted light microscopy, powder X-ray diffractometry (XRD), and electron probe microanalysis (EPMA).

[10] Optical microscopy was used to identify trace minerals and noncrystalline phases that would be undetected by XRD analyses. Representative subsamples of the hydrothermal encrustations were sent to High Mesa Petrographic in Los Alamos, NM where double polished thin sections were made. Subsamples were impregnated with epoxy, and cut across distinctly colored mineral layers (see Figure 6) to provide a cross-sectional view of the different mineral zones present in the samples. Petrographic relationships were observed in thin sections with a polarizing optical microscope, using both reflected and transmitted light.

[11] XRD analyses were used to identify the dominant crystalline phases. In preparation for XRD analysis, the hydrothermal deposits were selectively subsampled by removing small amounts of material from visually distinct mineral zones (Figure 6). Subsampled material was ground to a fine (2–10 micron) powder, and mounted onto a glass slide. Separation of a <2 micron phyllosilicate fraction was achieved by centrifuging. The phyllosilicate separates were mounted as packed unoriented powders and as oriented slurries on glass slides. Duplicate oriented slides were treated with ethylene glycol to expand the basal spacings of any swelling phyllosilicates that might be present [*Jackson*, 1969]. All of the slides were then analyzed using

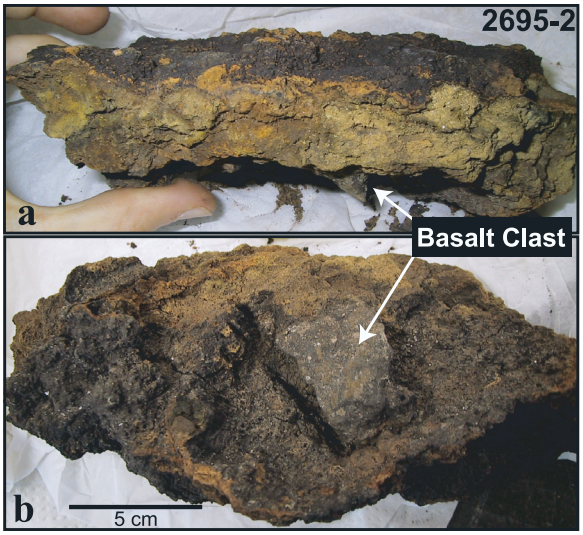

Figure 3. Photos of mineralized breccia sample 2695-2 from Tevnia Site, showing two views of a large basalt clast embedded in the sample. Note that Figure 3a exhibits the same sequence of compositional layering observed in the Ochre Site sample shown in Figure 6.

Figure 4. Macrofauna images photographed during *Alvin* dive 2695. (a) Carbonate shell of a dead bivalve observed near Ochre Site. Bivalves known to inhabit the East Pacific Rise are vent-endemic organisms. At depths ≥2500 m the shells of these organisms dissolve postmortem in a relatively short time (in less than a few hundred years). (b) Shrimp swimming over a region of hydrothermal mineralization at Tevnia Site; unknown species (may or may not be vent-endemic). (c) Galatheid crab (commonly called "squat lobster") photographed near Tevnia Site; although the unidentified species shown is not known to be vent-endemic, this group is common and abundant at active hydrothermal vents.

a Philips X' Pert powder X-ray diffractometer, and Cu Kα radiation. A scan speed of 0.040 degrees/s and a 20 mA current was used in every case except for the phyllosilicate separates, which were analyzed at a slower scan speed (0.020 degrees/s) and higher current (40 mA) to improve peak resolution of indistinct peaks.

[12] A five-spectrometer electron microprobe (Cameca model SX-50) was used to gather quantitative chemical data for calculation of a unit-cell formula for the phyllosilicate component. Multiple points were analyzed in target areas where microcrystalline phyllosilicate was identified optically on a polished thin section of sample 2695-4-1a.

4. Sample Descriptions and Petrographic Features

4.1. Tevnia Site Samples

[13] Samples 2695-1 and 2695-2 are very similar samples recovered from the western, axis-facing fault scarp at Tevnia Site (Figures 1, 2, and 3). For each sample, a summary description is provided in Table 1a, and a list of the minerals identified in the samples is provided in Table 1b. With varying degrees of distinctness, the hand samples grade from a friable, greenish-yellow phyllosilicate to a yellow-orange hydrous Fe-oxide zone to a dark-brown, indurated Mn-oxide crust (Figure 3).

[14] The Tevnia Site samples are breccias composed of volcanic, hydrothermal, and biogenic components (Figures 3, 7, and 8). The fine-grained matrix is composed largely of oxidized Fe-minerals, spherulitic opaline silica, and microfossiliferous sediment (Figure 7a). Inclusion of sediment components in the matrix establishes that mineralization occurred on the exposed scarp, rather than within the seafloor. Enclosed in this matrix are clasts of basaltic rock fragments, glass shards, and composite microbreccia fragments internally cemented by hydrothermal precipitates (Figure 7b). Brecciation in these samples occurs at the microscale to macroscale: Figure 3 shows a large basalt

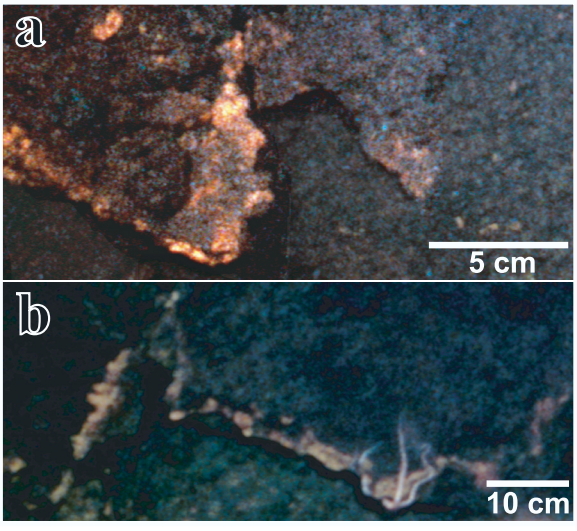

Figure 5. (a and b) *Alvin* 35-mm film images of hydrothermal encrustations at Ochre Site. Note that yellow mineral layer corresponds with Layer II in Figure 6 (zone of hydrous Fe-oxide + amorphous silica). The jagged exposures of this zone have been produced where fragile ledges of the hydrothermal crusts have broken away. The uppermost dark-colored layer of material corresponds to Layer III in Figure 6 (zone of Mn-oxide minerals).

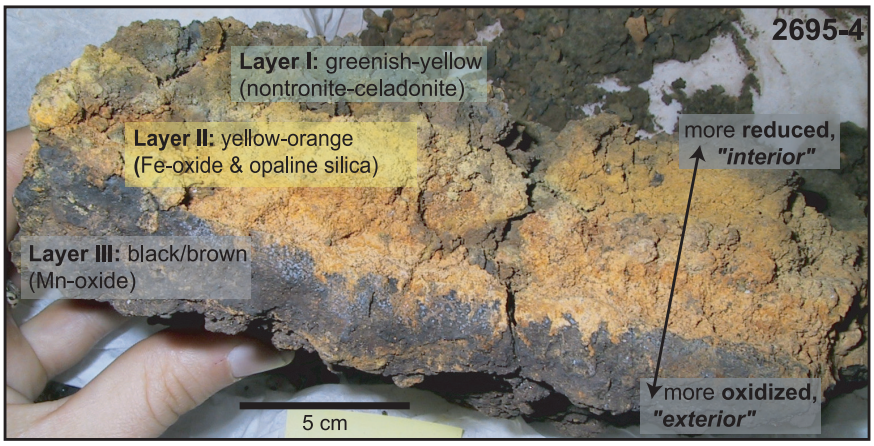

Figure 6. Photograph of sample 2695-4 from Ochre Site shows distinct layering from Layer I (= ''interior'' zone in contact with basaltic substrate) to Layer III (= ''exterior'' zone at the interface with bottom seawater). Layer I is a friable greenish-yellow colored zone composed of mixed layer nontronite (Fe-smectite) and celadonite (hydrous ferroan mica); Layer II is a yellow-orange zone of hydrous Fe-oxide + amorphous silica; Layer III is an indurated black-brown layer composed of Mn-oxide minerals (birnessite/todorokite). These mineral zones likely equilibrated along a mixing gradient between oxygen-depleted hydrothermal fluid and oxygenated seawater.

fragment embedded in sample 2695-2. Optical microscopy reveals that the Tevnia Site breccia samples contain at least three generations of tectonic brecciation and hydrothermal cementation (Figure 9). The photomicrograph in Figure 9a shows an elongate microbreccia clast cemented by a fine-grained hydrothermal matrix. In this example, the matrix of the microbreccia is the ''first generation'' of hydrothermal cementation. The microbreccia clast is in turn embedded in the ''second generation'' hydrothermal cement which composes the dominant matrix of the sample. A crack extends through the coherent microbreccia clast and is in-filled by a ''third generation'' of hydrothermal precipitation, shown in detail by Figure 9b. Figures 9c and 9d show a throughgoing crack which cuts across the ''second generation'' cement and is then capped by a ''third generation'' of hydrothermal material at its terminus (magnified in Figure 9d). Figure 9c also shows the microbreccia clast featured in Figure 7b (denoted with an asterisk) adjacent to a crack which bisects the sample. The absence of subsequent hydrothermal cementation within or at the termination of this crack suggests that it may represent the most recent cracking event.

[15] In thin section, a greenish-yellow mineral phase forms alteration rinds around included basalt clasts and is present at the edges of glass shards (Figures 10a–10d). In the matrix, the same alteration mineral occurs massively in relatively homogeneous zones, often commingled with opaline silica and fine-grained oxidized Fe-minerals. This mineral has the appearance of a cryptocrystalline phyllosilicate that retains a greenish-yellow color in cross-polarized light. Yellow staining from oxidized Fe-minerals likely augments the strong coloration of the phyllosilicate mineral. The phyllosilicate is identified as a mixed layer non-

Table 1a. Description of *Alvin* Dive 2695 Hand Samples and Polished Thin Sections

Sample	Hand Sample Description	Petrography of Polished Thin Sections
1	irregularly shaped fragments (1–5 cm pieces); thin layering evident but discontinuous & irregular	matrix/cement composed of Fe-oxide + silica + celadonite-nontronite; clasts include forams + other microfossils + mm-sized crystalline basalt & glass fragments + microbreccia clasts
2	flat sample (22 cm long × 5 cm thick); exhibits distinct colored layers; 5 cm basalt fragment embedded into it; see Figure 3	matrix/cement composed of Fe-oxide + silica + celadonite-nontronite; clasts are forams + other microfossils + crystalline basalt & glass fragments + microbreccia clasts
4	thick sample (12 cm long × 8 cm thick); exhibits distinct colored layers (each ~2–3 cm); friable; see Figure 6	nontronite -celadonite w/ birnessite ± todorokite filling fractures

Table 1b. Minerals Identified in *Alvin* Dive 2695 Samples by Powder X-Ray Diffractometry (XRD)

Sample	Subsample	Subsample Description	Minerals
1	A	black crust "exterior"[a]	[amorphous][b]
	B	black/green "interior"[a]	poorly crystallized nontronite-celadonite
	C	sooty dark layer	[amorphous] w/ possible nontronite-celadonite peaks
	D	reddish "interior"[a]	[amorphous][b]
	E[c]	black/green "interior"[a]	birnessite + nontronite-celadonite
2	A	black crust "exterior"[a]	poorly crystallized nontronite-celadonite
	B	black layer (sandwiched between orange & yellow layers)	nontronite-celadonite
	C	yellowish "interior"[a]	nontronite-celadonite
4	A	hard greenish nodule "interior"[a]	nontronite-celadonite
	B	shiny, hard back layer (at interface w/ orange layer)	todorokite + birnessite
	C	orange layer	[amorphous][b]
	D	black crust "exterior"[a]	birnessite (+less todorokite than XRDb)
	E	yellow-green nodule	nontronite-celadonite
	F[c]	yellow w/ greenish-blue nodule	well-crystallized nontronite-celadonite
	G[c]	hard black layer (at interface w/ orange layer)	birnessite (+minor nontronite-celadonite)

[a] "Exterior" used here to describe the black Mn-oxide encrusted side of a sample in direct contact with seawater, while "interior" is the opposite (under) side, usually greenish-yellow and dominated by phyllosilicate minerals; see Figures 5 and 6.
[b] No distinct diffraction peaks observed with Cu-K α radiation (i.e., amorphous).
[c] Subsamples mechanically separated to isolate the $<2\mu$ fraction.

tronite-celadonite on the basis of crystal structure and composition (see sections 6.1 and 6.2), and apparently corresponds to the greenish-yellow layer identified as Layer I in the hand samples (see example of layering in Ochre Site sample shown in Figure 6).

4.2. Ochre Site Samples

[16] Sample 2695-4 (Figure 6) was collected from the eastern side of the abyssal hill at Ochre Site (see Figures 1 and 5, Tables 1a and 1b). This sample does not contain volcanic or biogenic sedimentary components. It is purely a hydrothermal precipitate with a mineral assemblage that is essentially the same as the hydrothermal component in the Tevnia Site samples. The greenish-yellow phyllosilicate is pervasive, and again is associated with colloform silica and some oxidized Fe-minerals (Figures 11a and 11b). Where this greenish-yellow phyllosilicate is concentrated in thin sections, a gridded pattern of undulatory extinction is observed in cross-polarized light and at low magnification that mimics the "tartan" extinction of twinned microcline (Figure 11a). Preferred growth orientation of phyllosilicate microcrystals may cause the anomalous extinction observed. In sample 2695-4, the phyllosilicate mineral has cracked and has been in-filled by an opaque mineral (Figures 11c and 11d). In reflected light this opaque secondary mineral exhibits a roughly concentric, onion-like habit (Figure 11d). Optical properties indicate that this in-fill is todorokite and/or birnessite. XRD data (section 6.1) show that both minerals are present. Sample 2695-4 exhibits a well-defined mineral zonation sequence. Figure 6 shows the succession of zones from (I) a more friable greenish-yellow layer, to (II) a yellowish-orange layer, to (III) a more indurated dark brown/black layer, with each zone spanning $\sim$10–20 mm. Between the yellowish-orange-colored layer and the black layer, there is a small band of shiny, hard, black material which gives way to the matte-colored bulk of the dark layer, eventually terminating at the edge of the sample with a relatively smooth black crust.

5. Fauna and Microfossil Descriptions

5.1. Fauna

[17] Several organisms reported and/or photographed from Tevnia and Ochre Sites are endemic to deep sea hydrothermal vent areas (e.g., *Tevnia* tube worms, bivalves, "dandelion" siphonophores) while others (e.g., galatheid crabs, microbial mats, shrimp) are common but more equivocal indicators of deep-sea hydrothermal activity (Figures 2 and 4).

[18] The *Tevnia* worms (discussed in section 2) provide direct evidence of recent hydrothermal

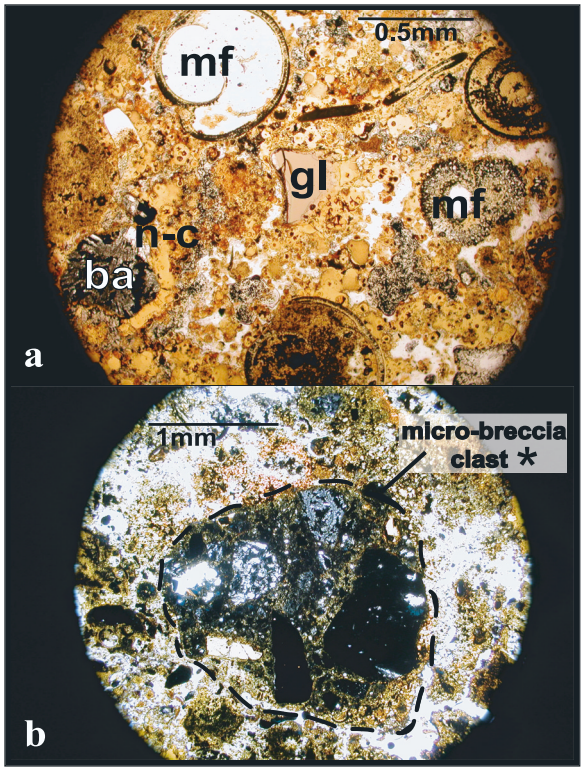

Figure 7. Photomicrographs in plane polarized light of thin sections from Tevnia Site showing composition and petrographic features of mineralized (Fe-Si-Mn) breccia deposits (sample 2695-1); ba, basalt fragment; mf, microfossil; gl, glass shard; n-c, hydrothermal nontronite-celadonite. Modified from *Haymon et al.* [2005]. (a) Fe- and Si-rich, yellow-orange zone (Layer II in Figure 6). The matrix is composed largely of porous hydrous Fe-oxide and spherulitic amorphous silica. (b) Microbreccia clast (enclosed by the dashed line; see also Figure 9c) composed of basalt fragments and glass shards internally cemented by a dense matrix of fine-grained hydrous Fe-oxide, amorphous silica, and opaque minerals.

activity on this young EPR abyssal hill. At the climax of hydrothermal flow, the fluids must have carried sufficient H_2S to sustain *Tevnia* individuals and their endosymbionts. However, as venting waned and fluid temperature dropped, a decrease in H_2S concentrations coupled with an increase in iron may have choked off the *Tevnia* colonies in a manner similar to the coupled vent fluid evolution and faunal succession previously observed by *Shank et al.* [1998] on the EPR axis at 9°50′N. Although the yellow-colored precipitate observed on and around the worm tubes at Tevnia and Ochre Sites (see Figure 2) was not sampled, this material may contain hydrous Fe-oxide, which was deposited on and around dying worm colonies at 9°50′N during this declining stage of venting [*Shank et al.*, 1998].

[19] *Alvin* video footage for dive 2695 shows moss-like microbial mats attached to basaltic outcrops. These microbial flocculations grow densely on the fault scarp and are pervasive around both Tevnia and Ochre Sites. Microbial floc observed growing on bare basalt substrate in ridge environments has been observed thus far only in association with hydrothermal vents. Similar-looking microbial floc, sampled in 2002 from an abyssal hill fault scarp 25 km west of the EPR axis at 9°27′N, contained a diverse assemblage of thermophilic and hyperthermophilic Archaea associated with high-temperature sulfide mineral particles, including chalcopyrite [*Haymon et al.*, 2005]. On the basis of these observations, *Haymon et al.* [2005] speculated that the microbes had been flushed out of a hot subseafloor biosphere thriving in hydrothermal reservoirs within the ridge flank. Abundance of microbial mats at Tevnia and Ochre Sites is consistent with the hypothesis that venting at these sites either was ongoing (but not visible), or had ceased only recently; however, without samples of the observed mats and the fluids that nourished them, it is not possible to infer the growth temperature of these mats, or the provenance of the microbes.

[20] At Ochre Site, an empty but intact bivalve shell was photographed on bare basalt at a depth of ~2795 m (Figure 4a). Although the bivalve was not positively identified, size and shape suggest that it may have been *Calyptogena magnifica,* a species endemic to hydrothermal vent environments. In a study by *Kennish and Lutz* [1999], the complete dissolution of an adult *C. magnifica* shell was estimated at ~300 years when located in the vicinity of a hydrothermal vent at ridge crest depth (2615 m); this dissolution rate is 20 times faster than the rates observed at non-vent ridge crest sites. Therefore persistence of this intact bivalve shell at 2795 m depth, where both carbonate undersaturation and acidic hydrothermal fluids would be expected to accelerate dissolution, is consistent with other observations suggesting that Tevnia and Ochre Sites are not fossil ridge-crest vents, but are instead recently active, abyssal hill vent sites.

5.2. Microfossils

[21] Pelagic and benthic microfossils were found only in the brecciated samples collected from the axis-facing fault scarp (Tevnia Site). Presence of

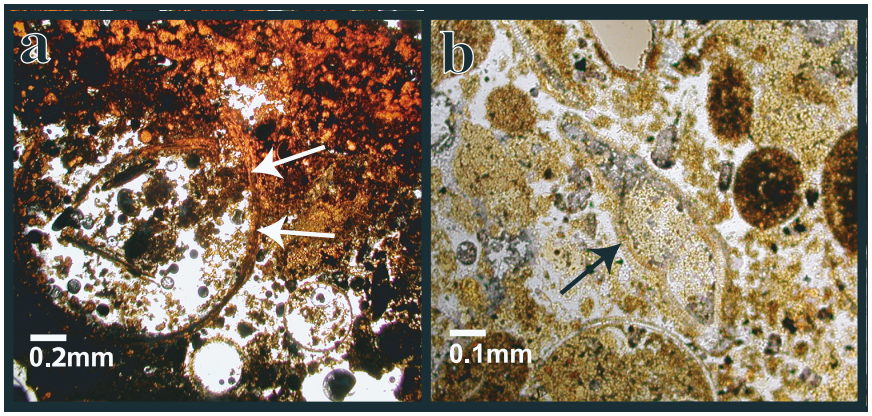

Figure 8. Photomicrographs in plane polarized light of thin sections from Tevnia Site breccia samples, showing fossils preserved by hydrothermal mineralization. (a) White arrows point to a possible fossilized worm tube in cross section (sample 2695-2). (b) Black arrow points to a benthic foraminiferan preserved by nontronite-celadonite (sample 2695-1).

this biogenic sediment component suggests that the hydrothermal precipitates from Tevnia Site formed over an extended period of time, gradually incorporating material from the steady rain of marine snow from above. The microfossil assemblage is dominated by forams (Figure 7a). Figure 12 is a series of photomicrographs from a hydrothermal sample showing the pattern of foram preservation

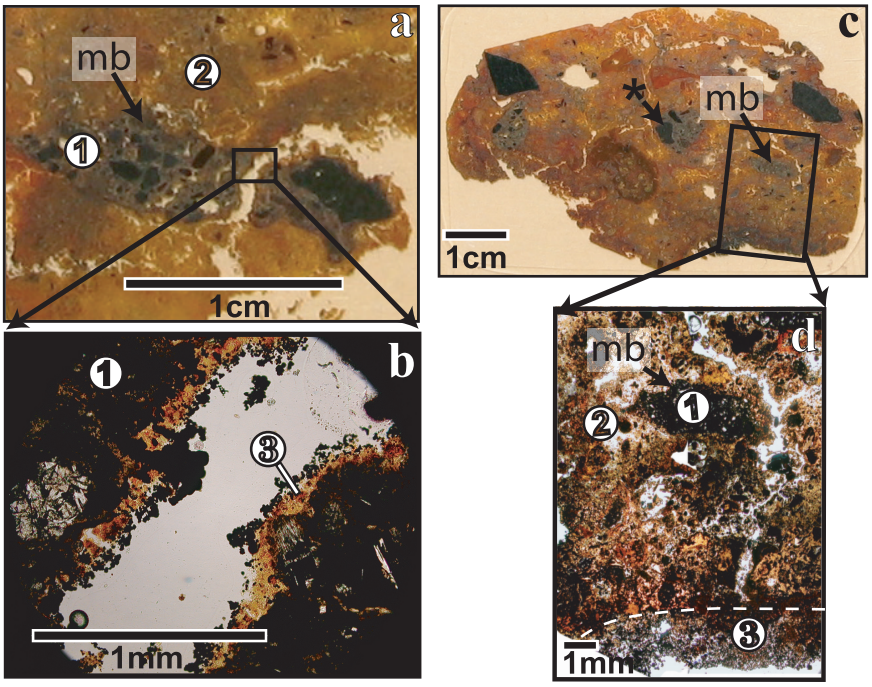

Figure 9. (a–d) Photomicrographs in plane polarized light of two Tevnia Site thin sections (from sample 2695-1) that exhibit at least three generations of brecciation and hydrothermal cementation; mb, microbreccia fragment; asterisk (*) denotes same microbreccia clast as shown in Figure 7b. Generations of hydrothermal cement are labeled 1, 2, and 3, where 1 is the first generation of hydrothermal precipitate, cementing microbreccia clasts which are embedded in cement 2, 2 is the second generation hydrothermal cement, composing primary matrix of the collected hand samples, and 3 is the third generation hydrothermal cement. Figure 9b shows the third generation cement filling a crack that is shown in Figure 9a cutting through both the first and second generation cements. Figures 9c and 9d also show at least three generations of hydrothermal recementing, including a layer of late mineral precipitates (below white dotted line in Figure 9d) that cap the terminus of a crack cutting through generation 2 matrix cement.

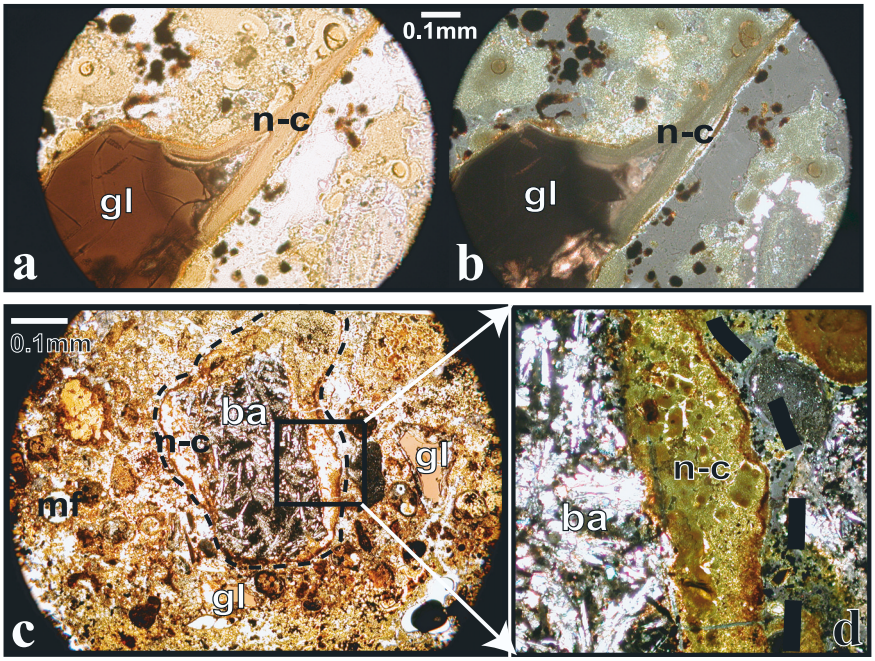

Figure 10. (a–d) Photomicrographs of thin sections from Tevnia Site breccia samples, showing the yellowish phyllosilicate mineral that was identified from XRD analyses (Figure 14) as a randomly interstratified mixed layer nontronite-celadonite. This mineral is pervasive throughout the Tevnia and Ochre Site samples. It is often associated with colloform silica and hydrous Fe-oxide and is most concentrated in the greenish-yellow colored "interior" Layer I (see Figure 6); n-c, nontronite-celadonite; gl, glass shard; ba, basalt clast; mf, microfossil. (a) Photomicrograph in plane polarized light showing nontronite-celadonite forming an alteration rim at the edges of a glass shard. (b Photomicrograph in cross polarized light showing same shard and alteration rim as in Figure 10a. (c) Photomicrograph in cross polarized light showing a basalt clast that is embedded in the hydrothermal matrix of sample 2695-1 and is rimmed by a rind of nontronite-celadonite (outlined with dashes). (d) Close-up photomicrograph of the boxed portion of the alteration rind shown in Figure 10c; cross polarized light.

across the mineral zones (representative of a redox gradient). In the hydrous Fe-oxide + silica zone (Layer II) the calcareous foram shell is well-preserved (Figures 12a and 12b); while in the more reduced nontronite-celadonite zone (Layer I), the foram tests are either dissolved out (Figures 12c and 12d) or replaced by nontronite-celadonite (Figures 12e and 12f). Other fossilized biota seen in thin sections may include worm tubes (Figure 8).

5.3. Fossilized Microbes

[22] A variety of microbe-like filamentous textures were observed in thin sections from the abyssal hill hydrothermal deposits. Figure 13 shows three of these microtextures, preserved in opaline silica and/or Fe-oxide. Although it has not been confirmed, a microbial origin for these microtextures seems likely. According to *Jannasch* [1995], precipitation of hydrothermal manganese is predominantly microbial, and other investigators describe similarly sized (1–2 μ diameter) filaments, attributable to hydrothermal microbes, coated by ferrihydrite and silica [e.g., *Juniper and Fouquet*, 1988; *Little et al.*, 2004]. Previous work has shown that microbes mediate ferrihydrite precipitation [*Edwards et al.*, 2004; *Boyd and Scott*, 2001; *Kennedy et al.*, 2003; *Emerson and Moyer*, 2002], and experimental study demonstrates that in Fe-rich solutions bacterial silicification may occur as a two step process: (1) Fe partitioning onto bacterial cells via sorption and surface precipitation, followed by (2) Si sorption/precipitation onto the Fe-coated bacterial surface [*Yee et al.*, 2002]. Preservation of microbial filaments by celadonite-nontronite (Figure 13c) has been described previously in samples from the southern Explorer Ridge [*Fortin et al.*, 1998].

6. Results of Mineral Analyses

6.1. XRD Results

[23] Minerals identified by XRD are summarized in Table 1b. On the basis of comparison of the peak patterns in the samples with the ICDD

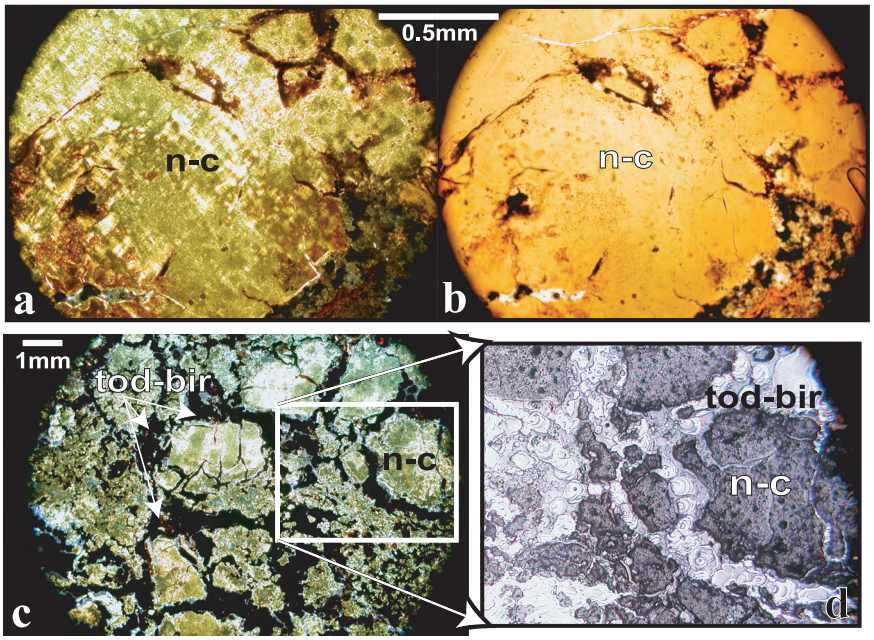

Figure 11. (a–d) Photomicrographs of thin sections from Ochre Site, sample 2695-4, showing randomly interstratified mixed layer nontronite-celadonite; n-c, nontronite-celadonite; tod-bir, todorokite-birnessite. (a) Photomicrograph in cross polarized light showing area of thin section where nontronite-celadonite is massive and relatively homogeneous. Anomalous pattern of undulatory extinction optically resembles microcline twinning but possibly is caused here by microcrystal growth orientation. (b) Photomicrograph in plane polarized light of same area shown in Figure 11a. (c) Photomicrograph in cross polarized light showing cracks in nontronite-celadonite (possibly formed from dehydration and contraction during hydrothermal reheating) that have been filled by opaque Mn-oxide (todorokite-birnessite). (d) Close-up photomicrograph in reflected light of the boxed area in Figure 11c, showing concentric, onion-like texture of Mn-oxide minerals that are filling cracks in nontronite-celadonite.

powder diffraction file database, we have identified the four distinctly colored/textured materials present in the samples as: a mixed-layer nontronite-celadonite (greenish-yellow smectite-mica phase, Layer I), X-ray amorphous silica and hydrous Fe-oxide (yellow-orange friable material, Layer II), and birnessite ± todorokite (dark-colored Mn-oxide material, Layer III). Figure 14 shows XRD patterns for the phyllosilicate separates, and Table 2 provides XRD data for the Mn-oxide minerals comprising Layer III. The fine-grained, ferric oxide phase in Layer II may be ferrihydrite but because of its X-ray amorphous structure, we simply refer to it as "hydrous Fe-oxide" [*Jambor and Dutrizac*, 1998].

[24] The greenish-yellow phyllosilicate is poorly crystalline, exhibiting broad XRD reflection peaks (Figure 14). A swelling smectite component is present, on the basis of expansion of the (001) basal d spacing after glycolation (from approximately 13Å to 16Å; Figure 14) and occurrence of a composite (060) peak at ~1.52Å. In different subsamples, the phyllosilicate basal reflections show irregular variation in intensity, and are sometimes absent. The peaks match or fall between peaks for nontronite and celadonite, indicating that the sample is a mixed-layer smectite-mica.

[25] If a mixed layer phyllosilicate is regularly interstratified, its basal reflections will be rational. To test for rationality in the basal reflections, basal d spacings were selected from a glycolated, nontronite-celadonite XRD pattern (2695-4f). These d spacings were used to calculate the coefficient of variability (CV) (Table 3) [*Bailey*, 1988]. The calculated CV values are greater than 0.75%, and therefore fall into the irrational category [*Bailey*, 1982] characteristic of an irregularly interstratified mixed-layer phase. Thus the greenish-yellow phyllosilicate appears to be an irregularly interstratified mixed-layer nontronite-celadonite. To check this identification, microprobe analyses on the phyllosilicate composition were conducted (see section 6.2).

6.2. EPMA Results

[26] Quantitative elemental analyses (acquired by EPMA) were obtained for the greenish-yellow

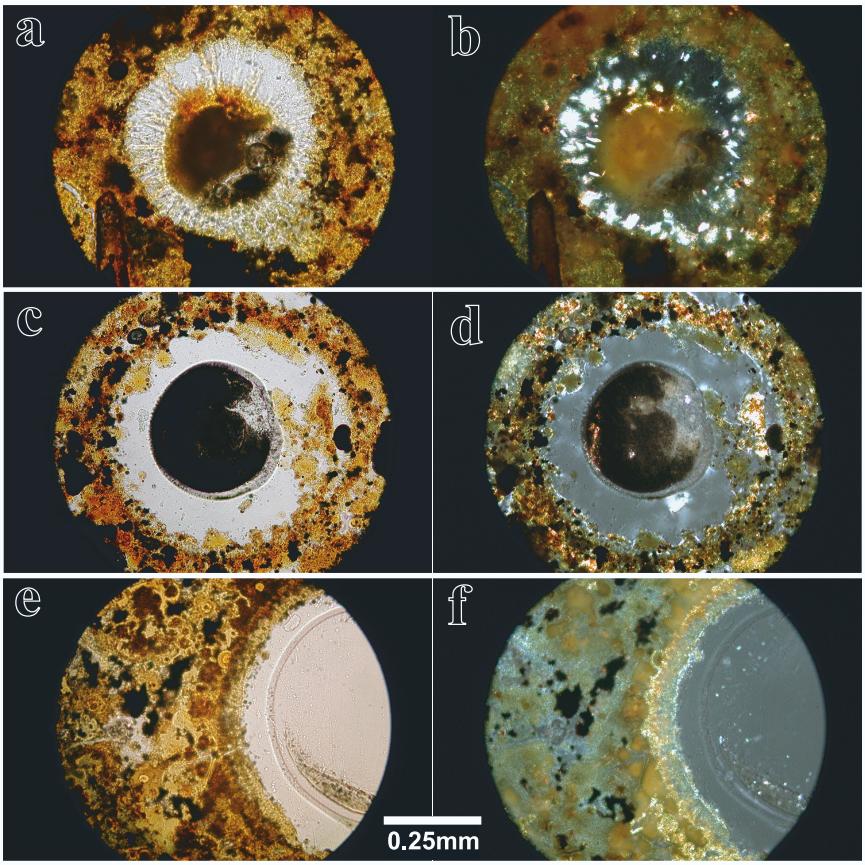

Figure 12. (a) Photomicrograph in plane polarized light showing calcite preserved in a foraminiferan fossil within the hydrous Fe-oxide + silica mineral zone (Layer II). (b) Same as Figure 12a; cross polarized light. (c) Photomicrograph in plane polarized light showing a void space where calcite foram shell has been dissolved by acidic fluids in the nontronite-celadonite mineral zone (Layer I). (d) Same as Figure 12c; cross polarized light. (e) Photomicrograph in plane polarized light showing replacement of calcite in the wall of a foram shell by nontronite-celadonite (in Layer I). (f) Same as Figure 12e; cross polarized light.

smectite-mica phyllosilicate. Major cation weight percent oxide values and atomic proportions are shown in Table 4. Oxides total to ~96%, leaving at most 4 wt.% attributable to water. Stoichiometry is based on 24 oxygen equivalencies. The iron-rich and aluminum-poor nature of this smectite-mica phyllosilicate is consistent with thin-section observations and XRD data (Figure 14), and points to a nontronite (Fe-smectite) and celadonite (Fe-mica) composition. The mica component was categorized as celadonite (rather than glauconite) on the basis of three criteria: (1) the dominance of Mg in the 2+ octahedral site, (2) tetrahedral Al (or Fe^{3+}) <0.2 atoms per formula unit, and (3) a contribution to the *d*(060) peak which appears to be <1.510Å (as recommended by the Clay Minerals Society Nomenclature Committee; see *Bailey et al.* [1979] and Figure 14).

[27] Stoichiometric formulas were calculated for these two phyllosilicates by first assigning the K and Mg to a standard celadonite formula of $K_2(Mg_2Fe_2)(Si_8)O_{20}(OH)_4$. Next, the remaining molar proportions were assigned to a nontronite formula, resulting in the following stoichiometry: $(\frac{1}{2}Ca_{0.04},Na_{0.69})(Mg_{0.01},Fe_{4.00})[(Si)_{7.10}(Fe_{0.90},Al_{0.02})\ O_{20}](OH)_4$ (see Table 4). On the basis of this formula, the calculated relative abundances of nontronite and celadonite in the mixed-layer phyllosilicate are 68% nontronite and 32% celadonite.

7. Comparison to Similar Seafloor Hydrothermal Deposits

[28] Most nontronite and Mn-oxide deposits previously recovered from ridge flanks occur on isolated volcanic seamounts [*Piper et al.*, 1975; *Batiza et al.*, 1977; *Lonsdale et al.*, 1980; *Malahoff et al.*, 1982; *Alt et al.*, 1985; *Marchig et al.*, 1999; *Boyd and Scott*, 2001]. These seamount hydrothermal

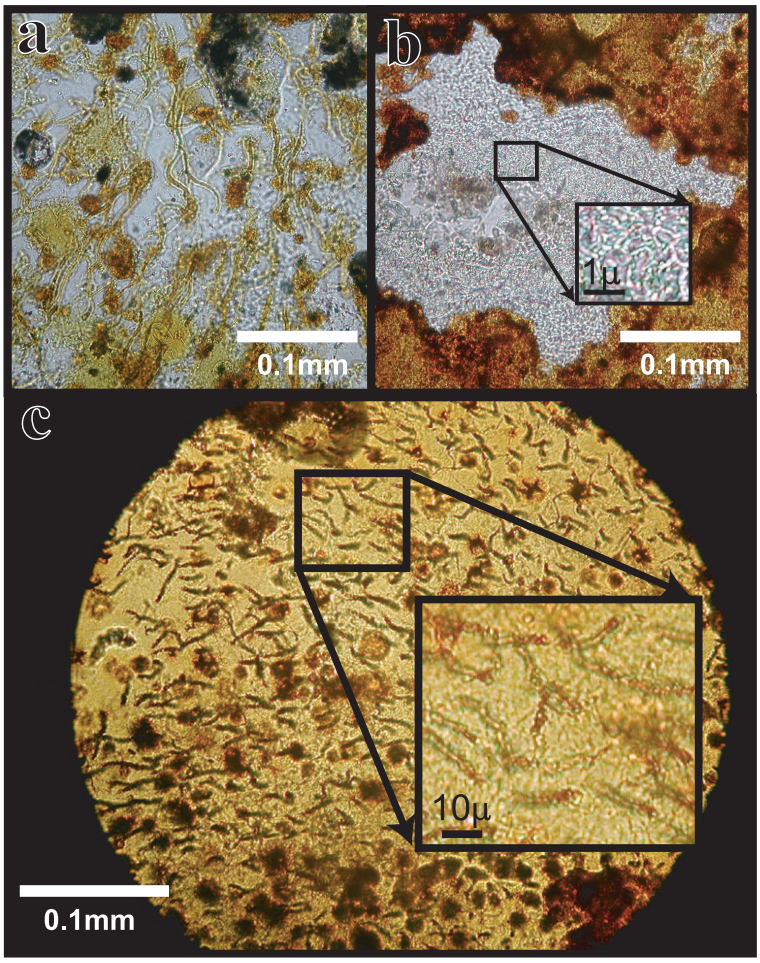

Figure 13. Thin section photomicrographs in plane polarized light from Tevnia Site breccia samples (2695-1 and 2695-2), showing microbial textures preserved by hydrothermal mineralization. Two sizes of microbe-like textures are found in both the oxidized (Layer II, III) zones and the more reduced zone (Layer I). (a) Filamentous microbe-like textures preserved in Layer II by Fe-stained amorphous silica. (b) Coral-like, anastomising texture within void space throughout the Tevnia Site samples, which appears to be a network of branching filamentous microbial fossils preserved in silica; note that these filaments are an order of magnitude smaller than those shown in Figures 13a and 13c; very fine opaque mineral grains are dispersed and suspended in the silica filament network. (c) Filamentous texture shown here may be microbial fossils preserved within Layer I nontronite-celadonite.

deposits are geochemically similar to the deposits we describe, but are not genetically comparable to abyssal hill deposits which have formed in amagmatic, tectonized, thinly sedimented settings. It is important to characterize tectonic abyssal hill hydrothermal systems, which are seldom-described yet are responsible for much advective cooling and alteration of ocean lithosphere. Therefore we compare the Tevnia Site and Ochre Site samples to other well-described examples of Fe-Si-Mn hydrothermal deposits from nonmagmatic ridge environments in Tables 4 and 5. The numbered columns in Table 4 correspond with the sites described in Table 5. The Fe-Si-Mn samples in Tables 4 and 5 all come from either (1) true ''off-axis'' locations, where seafloor age is at least 0.1 Ma (columns 1 and 2), or (2) sites on medium- to slow-spreading ridge crests (columns 3–7) that are magma-starved, faulted, and may host hydrothermal systems similar to fault-controlled ridge flank systems. At these nonseamount mid-ocean ridge sites, hydrothermal deposits exhibit mineral assemblages and layering strikingly similar to the deposits in this study. Specifically, this class of hydrothermal deposits grades from an ''interior'' zone of Fe-silicate (nontronite ± celadonite or glauconite), to a hydrous Fe-oxide and opaline silica-dominated zone, terminating with an ''exterior'' Mn-oxide zone

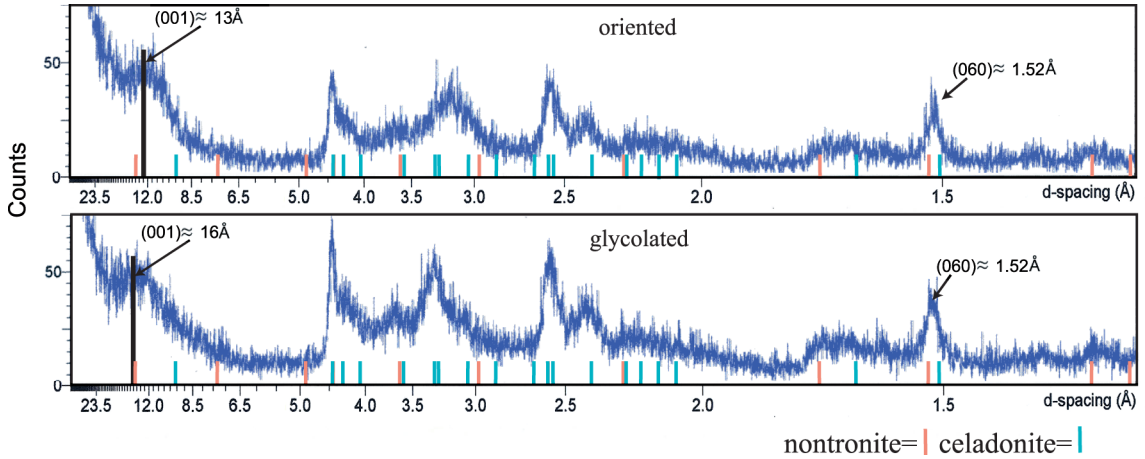

Figure 14. Powder X-ray diffraction (XRD) patterns for the phyllosilicate phase (<2 μ fraction) separated from the greenish-yellow material in Layer I (Figure 6). *X* axis = # detected counts; *Y* axis = d spacing (in Å). (top) Untreated, oriented slide shows a smectite basal spacing of 13 Å. (bottom) Ethylene glycol treated slide exhibits a smectite basal spacing expansion to 16 Å. Stick patterns show ICDD-PDF d spacings for nontronite in red (ICDD-PDF file 34-0842) and celadonite in cyan (ICDD-PDF file 17-0521). Observed peaks fall on or between peaks for nontronite and celadonite and are consistent with identification of an irregular mixed layer nontronite-celadonite phase.

(birnessite and/or todorokite). This mineral zonation sequence is thought to form from mineral precipitation along a mixing gradient between reduced, Fe-rich hydrothermal fluid and oxygenated seawater [*Grill et al.*, 1981]. The effective segregation of Fe and Mn along a redox gradient created by mixing distinguishes these hydrothermal samples from unfractionated hydrogenous marine ferromanganese deposits that form ubiquitously on the seafloor at low temperatures [*Corliss et al.*, 1978; *Grill et al.*, 1981; *Boyd and Scott*, 2001].

[29] Among the deposits described in Tables 4 and 5, the Galapagos Mounds most closely resemble our EPR abyssal hill samples in composition, age and geologic setting. However, the Galapagos Mounds were deposited within a blanket of pelagic sediment that covers an abyssal hill fault

Table 2. Powder X-Ray Diffraction Data for Well-Crystallized Mn-Oxide

Layer IV[a] Sample 2695-4 b Birnessite and Todorokite[b]				
d Spacing, Å	Angle, °2θ	Relative Intensity, %	Todorokite, hkl	Birnessite, hkl
13.43	6.588	45	non-cel[c]	non-cel
9.844	8.98	100	100, 001	-
7.285	12.14	97	-	002
4.935	17.96	51	200	-
3.548	25.08	45	-	212
3.304	26.97	25	non-cel, 300, 202	-
2.449	36.67	50	401, 211, 112, 004	144, 161
1.798	50.74	20	-	316, 433, 181
1.706	53.69	56	non-cel	non-cel
1.643	55.93	9	?	?
1.620	56.80	16	-	461
1.544	59.87	27	non-cel	non-cel, 119, 0101, 347
1.416	65.91	29	020	611
1.290	73.33	14	?	?
1.276	74.26	10	?	?

[a] See Figure 6.
[b] Includes minor phyllosilicate component (nontronite-celadonite).
[c] Non-cel = admixed nontronite-celadonite component responsible for or contributing to peak.

Table 3. Coefficient of Variability (CV) Values for the Mixed-Layer Phyllosilicate in Abyssal Hill EPR Samples[a]

Apparent Order	d Spacing[b]	Apparent Order × d	[mean − (order × d)]^2	CV
1	16.25	16.25	1.24	
2	7.45	14.90	0.06	
3	5.00	15.00	0.02	
4	3.74	14.96	0.03	
6	2.43	14.58	0.31	
		15.14[c]	1.66[d]	
			0.644[e]	4.25%[a]

[a] CV = 100 × (standard deviation/mean); *Bailey* [1982, 1988].
[b] For glycolated subsample 2695-4f.
[c] Mean value of (apparent order × d).
[d] Sum of [mean − (order × d)]^2.
[e] Standard deviation = [sum/(N − 1)]$^{1/2}$.

in ~600 Ka seafloor [*Lonsdale*, 1977; *Natland et al.*, 1979]. The active Galapagos Mounds have been forming over the past 100-300 Ky, and did not begin to form until the crust was already at least 200 Ky old and already buried by sediment [*Williams et al.*, 1979; *Honnorez et al.*, 1983; *Lalou et al.*, 1983; *Buatier et al.*, 1989]. Sedimentation has played an important role in the thermal history of the Galapagos Mounds, which clearly is not the case at Tevnia and Ochre Sites.

[30] Only our EPR samples (column 1 in Tables 4 and 5) and those collected from the Galapagos Mounds and the MAR FAMOUS area (columns 2 and 4) reportedly contain an Fe-mica phase (celadonite or glauconite). Table 4 shows that the nontronite phases are all chemically similar, exhibiting particularly high Fe and low Al content. The East Pacific Rise (this study) and the Galapagos Mounds (the two ''true off-axis'' sites, see Tables 4 and 5) exhibit the lowest aluminum values. Low Al and Mg indicates that iron is occupying some tetrahedral sites as well as nearly all of the octahedral sites [*Bischoff*, 1972; *Goodman et al.*, 1976] (Table 4). Low Mg and high Fe suggests that the nontronite precipitated from Mg-depleted and metal-enriched hydrothermal fluid that was largely undiluted by Mg-rich seawater.

8. Prior Experimental and Isotopic Studies of Nontronite and Celadonite Formation

8.1. Nontronite

[31] The majority of marine smectites are formed authigenically by three primary processes outlined by *Cole and Shaw* [1983]: alteration of volcanic rocks and glass (<20°C), formation from biogenic silica and Fe-oxyhydroxides at ambient bottom water temperatures, and direct precipitation out of low to moderate temperature (<150°C) hydrothermal fluids. Laboratory synthesis experiments as well as examination of authigenic marine smectites indicate that Fe-smectite (nontronite) forms under a wide range of temperature and redox conditions.

[32] *Harder* [1976, 1978] found that nontronite could be precipitated at ambient seafloor temperatures either from reducing solutions rich in ferrous iron, or under initially oxidizing followed by reducing conditions. However, more recent studies [*Decarreau and Bonnin*, 1986; *Decarreau et al.*, 1987] have shown that at 75°C a ferric dioctahedral smectite forms by nucleation under initially reducing conditions (as a ferrous stevensite) followed by rapid nontronite crystal growth upon sudden exposure to oxygen in air [*Decarreau and Bonnin*, 1986]. In another laboratory experiment, nontronite formed under strictly oxidizing conditions at elevated temperatures over an extended period (12 days at 100°C and 1 month at 150°C) [*Decarreau et al.*, 1987]. This work is in agreement with *Harder* [1976, 1977, 1978], who found that under oxidizing conditions nontronite cannot be synthesized at temperatures between 3° and 80°C. Oxygen isotopic data from naturally occurring seafloor hydrothermal nontronites show formation temperatures ranging from 3° to 140°C [*Cole and Shaw*, 1983; *Murnane and Clague*, 1983; *Corliss et al.*, 1978; *Barrett and Friedrichsen*, 1982; *McMurtry and Yeh*, 1981; *McMurtry et al.*, 1983].

8.2. Celadonite and Mixed Layer Nontronite-Celadonite

[33] Celadonite occurs as an alteration product and as a vein-filling precipitate in basaltic ocean crust. Celadonite is usually thought to be a product of low-temperature oxidative reaction between basalt and seawater [*Seyfried et al.*, 1978; *Alt*, 1995]. This interpretation is based on oxygen isotope formation temperatures ≤40°C for vein celadonite in seafloor drill cores [*Kastner and Gieskes*, 1976; *Seyfried et al.*, 1978; *Bohlke et al.*, 1984], and on a close association of celadonite with Fe-oxyhydroxide [*Seyfried et al.*, 1978; *Alt*, 1995]. However, celadonite + Fe-oxide also can form when K- and Fe-rich hydrothermal fluids cool and/or mix with seawater within volcanic host rocks. Studies of upper crust basalt alteration at ODP Site 801 (created at a fast spreading ridge) and at Hole 504b (created at an intermediate-rate spreading ridge)

Table 4. Chemical Compositions and Formulas for Fe-Smectites in Nonseamount Seafloor Hydrothermal Fe-Si-Mn Deposits[a]

	Off-Axis Sites			Magma-Starved Ridge Crest Sites			
	1	2	3	4	5	6	7
Phyllosilicate[b]	Nontronite-Celadonite (This Study)	Nontronite-Glauconite	Nontronite	Smectite or Nontronite + "Hydromica"[c]	Nontronite	Nontronite	Nontronite
Sample	2695-4 1a (average)	N2	24(d)	cyp 74-26-16	69-11-2	11G (XRF)	1243-1
Weight % Oxides							
SiO_2	51.27	53.0	46.9	44.4	46.4	46.7	26.0
Al_2O_3	0.08	0.04	0.19	0.2	1.59	0.32	0.09
Fe_2O_3	36.52	33.1	32.7	35.6	29.3	33.3	46.3
FeO	-	-	-	-	0.11	0.4	-
MnO	0.04	0.23	0.13	3.88 (Mn_3O_4)	0.29	0.04	0.87
MgO	3.01	2.8	3.22	2.84	3.22	2.8	3.08
CaO	0.19	0.11	0.66	0.8	0.50	0.4	0.24
Na_2O	1.69	1.39	1.71	1.84	1.07	1.0	-
K_2O	3.47	2.24	4.30	3.35	2.87	3.4	1.61
P_2O_5	0.04	-	-	-	-	0.04	-
TiO_2	0	-	-	0.02	0.13	0.02	1.57
Total	96.3	-	89.86	99.66	-	-	
Atomic Proportions	Celadonite 32%[d]	Nontronite 68%[e]	Nontronite	Nontronite		Nontronite	Nontronite	Nontronite
Tetrahedral layer								
Si^{4+}	8.0	7.10	7.74	7.32	-	7.44	7.325	-
Al^{3+}		0.02	0.007	0.03	-	0.30	0.058	-
Fe^{3+}		0.90	0.25	0.65	-	0.26	0.617	-
Sum	8.0	8.02	8.00	8.00	-	8.00	8.00	-
Octahedral layer								
Al^{3+}		-	0.00	-	-	0.00	0.000	-
Fe^{3+}	2.0	4.00	3.39	3.19	-	3.27	3.313	-
Fe^{2+}	-		-	-	-	0.02	0.053	-
Mg^{2+}	2.0	0.01	0.62	0.75	-	0.77	0.655	-
Mn^{2+}	-	-	-	-	-	0.04	0.006	-
Ti^{4+}	-	-	-	-	-	0.02	0.002	-
Sum	4.0	4.01	4.01	3.94	-	4.12	4.03	-
Interlayer cations								
$\frac{1}{2}$ Ca^{2+}	-	0.04	0.04	0.055	-	0.18	0.134	-
Na^{+}	-	0.69	0.39	0.52	-	0.32	0.303	-
K^{+}	2.0	-	0.42	0.86	-	0.58	0.680	-
Sum	2.0	0.74	0.85	1.44	-	1.08	1.12	-
Excess Layer Charge	-	-	0.86	-	-	1.01	1.30	-

[a] Note: Numbered columns correspond with site locations described in Table 5.
[b] According to source publications, Table 5.
[c] "Hydromica" = celadonite or glauconite.
[d] Celadonite = $K_2(Mg_2Fe_2)(Si_8)O_{20}(OH)_4$.
[e] Nontronite = $(\frac{1}{2}Ca_{0.04},Na_{0.69})(Mg_{0.01},Fe_{4.00})\ [(Si)_{7.10}(Fe_{0.90},Al_{0.02})\ O_{20}](OH)_4$.

both show that the earliest alteration assemblage consists of celadonite, mixed-layer celadonite-smectite, Fe-oxyhydroxide, and quartz [*Alt and Teagle*, 2003]. Oxygen isotope values for vein quartz and vein celadonite in Site 801 core samples yield calculated formation temperatures ranging up to 95°C for quartz and up to 67°C for celadonite. Maximum calculated temperatures are in veins near the bottom of the borehole, at 410–445 m of penetration into volcanic basement (above the volcanic/dike transition zone). Celadonite formation temperatures at Site 801 were calculated using the illite-water fractionation factor from *Savin and Lee* [1988] and by assuming equilibration with ambient seawater having $\delta^{18}O$ = 0‰ [*Alt and Teagle*, 2003]. However, equilibration with $\delta^{18}O$-

Table 5. Geologic Settings of Nonseamount Seafloor Hydrothermal Fe-Si-Mn Deposits

	True "Off-Axis" Sites		Magma-Starved Ridge Crest Sites				
Spreading Center	1 East Pacific Rise (This Study)	2 Galapagos Rift (Galapagos Mounds)	3 Gulf of Aden	4 Mid-Atlantic Ridge (FAMOUS Area)	5 Explorer Ridge	6 Juan de Fuca Ridge (Cobb Offset)	7 Mid-Atlantic Ridge (TAG Field)
Latitude and longitude	10°20′N, 103°33′W	00°35′N, 86°10′W	12°34′N, 47°39′E	37°N, 33°04′W	50°5′N, 129°45′W	47°35′N, 128°58′W	26°8″N, 44°48″W
Full spreading rate	10.9 cm/y [*Carbotte and Macdonald*, 1992]	~7 cm/y [*Klitgord and Mudie*, 1974]	~1 cm/y [*DeMets et al.*, 1990, 1994]	~2 cm/y [*DeMets et al.*, 1990, 1994]	~2 cm/y [*DeMets et al.*, 1990, 1994]	~6 cm/y [*Murnane and Clague*, 1983]	2.6 cm/y [*McGregor et al.*, 1977]
Reference(s)	this study	*Lonsdale* [1977]; *Natland et al.* [1979]; *Corliss et al.* [1978]; *Moorby* [1983]; *Maris et al.* [1984]; *Honnorez et al.* [1981, 1983]; *Klinkhammer et al.* [1977]; *Williams et al.* [1979]; *Buatier et al.* [1993]	*Cann et al.* [1977]	*Hoffert* [1978]	*Grill et al.* [1981]	*Murnane and Clague* [1983]	*Thompson et al.* [1985]
Location	~5 km E of EPR axis	~20 km S of GSC axis	~3 km N of MOR axis	Transform Fault A	37 km from actively spreading Western Rift	2.5 km W of projected MOR axis (propagating ridge segment)	MAR rift valley wall
Depth	~2900 m	~2700 m	2260–2550 m	~2700 m	~3000–3200 m	-	2500–3500 m
Age	deposits <100,000 y	deposits ~300,000 y max.; seafloor ~600,000 y	seafloor ~100,000 to 300,000 y max.	deposits ~45,000 y max; seafloor ~1 Ma	deposits prob. <10,000 yseafloor ~250,000 y max.	-	seafloor ~1 Ma
Depositional surface	bare basalt	20–30m of calcareous-siliceous ooze	bare basalt and sediment	carbonate sediment	unknown	bare basalt	carbonate ooze
Tectonic environment	active, exposed abyssal hill normal fault scarp	abyssal hill normal fault scarps	series of en echelon lateral slip faults in median rift valley	active transform fault zone	median ridge of inactive Eastern rift	OSC (overlapping spreading center)	east wall of rift valley
Fluid temperature (from oxygen isotopes)	-	3–20°C [*Corliss et al.*, 1978] 19–32°C [*Barrett and Friedrichsen*, 1982]	-	-	-	~57°C	-
Temperature (observed anomalies in seawater or sediments)	none	2°C/m gradients	-	none	-	-	-

enriched hydrothermal fluids would shift the calculated formation temperatures to slightly higher values. By substituting a reasonable range of hydrothermal fluid δO^{18} values (i.e., 0.4 to 2.13‰ at 9–10°N on the EPR axis [*Shanks et al.*, 1995]), formation temperatures from 72–87°C are obtained for pure celadonite; for mixed layer nontronite-celadonite, higher formation temperatures are possible, increasing with an increased smectite component up to the maximum temperature for pure nontronite (~150°C).

[34] Early-formed celadonite-nontronite in ocean crust thus may be largely hydrothermal in origin, with a basaltic source for both K and Fe, rather than a product of low temperature seawater-basalt interaction. Glauconite-nontronite also is known to form from reaction of hydrothermal fluid with pelagic sediment in the Galapagos Mounds [*Buatier et al.*, 1989].

[35] We conclude from existing experimental and isotopic data that nontronite can form at temperatures up to 150°C in hydrothermal environments that evolve or fluctuate in oxidation state. Celadonite is known to form at temperatures up to at least 70°C. Additional work is needed to establish the maximum formation temperature possible for hydrothermal nontronite-celadonite, but on the basis of the existing data for nontronite and celadonite we estimate that this maximum temperature lies between 70–150°C.

9. Inferred EPR Abyssal Hill Fluid Properties and Fluid Source

[36] Temperature and composition of EPR abyssal hill hydrothermal fluids at the Tevnia and Ochre Sites can be inferred from the precipitated mineral assemblage, and from the presence of *Tevnia* tubeworms.

[37] The temperature of the fluids was most likely <150°C, based on the phyllosilicate phases present, and almost certainly was <200°C, based on the absence of Zn and Cu minerals. At discharge temperatures above 200°C, Zn and/or Cu are mobilized and precipitated in seafloor hydrothermal deposits [*Haymon and Kastner*, 1981; *Crerar and Barnes*, 1976; *Janecky and Seyfried*, 1984; *Seyfried and Ding*, 1995]. At the Galapagos Mounds, where Fe-Si-Mn hydrothermal mineral deposits strongly resembling the EPR abyssal hill samples have formed, calculated oxygen isotope formation temperatures for opaline silica fall between 60–172°C [*Skirrow and Coleman*, 1982] and temperatures calculated from heat flow measurements are estimated at ~30°C [*Becker et al.*, 1983]. Geochemical modeling of seawater-hydrothermal fluid mixing indicates that at temperatures ranging from 50–200°C, mixtures of ridge crest hydrothermal fluids and seawater become saturated with respect to amorphous silica [*Janecky and Seyfried*, 1984]. We have not determined oxygen isotope formation temperatures for the silicate minerals in the EPR abyssal hill samples because it is very difficult to separate the silicates from one another and from finely dispersed oxide phases. However, on the basis of all of the foregoing observations, we conclude that the mineral assemblage at Tevnia and Ochre Sites must have formed from fluids <150°C.

[38] The mineral zonation sequence from nontronite-celadonite → hydrous Fe-oxide + silica → Mn-oxide observed in Tevnia Site breccia samples also is observed at other sites described in Table 5. *Corliss et al.* [1978] proposed that at the Galapagos Mounds, Gulf of Aden, and Mid-Atlantic Ridge (MAR) "FAMOUS" hydrothermal sites, pelagic sediment cover allowed nontronite to precipitate under reducing conditions beneath a cap of ferromanganese oxide formed at the sediment-seawater interface. In bare-basalt hydrothermal settings like the Tevnia and Ochre Sites, mixing at the rock/water interface between reduced fluids in volcanic basement rock and oxygenated seawater provides the spontaneous shift in redox conditions described by *Decarreau and Bonnin* [1986] required to convert ferrous stevensite to nontronite, and creates an O_2 gradient that explains the zonation observed from Mn-oxide in the "exterior" zone (in contact with seawater) to nontronite-celadonite in the "interior" zone (in contact with basalt). The presence of the *Tevnia* worm tubes is an independent indicator that the end-member hydrothermal fluids were reducing enough to transport H_2S. Although most of the calcareous microfossils observed in these samples have been replaced with hydrous Fe-oxide, some preservation of $CaCO_3$ fossils is observed within the Fe-oxide layer, but not in the nontronite-celadonite zone (Figure 12). These observations are consistent with the hypothesis that the observed mineral zonation sequence developed along a mixing gradient between lower-pH, more reducing hydrothermal fluid and more alkaline, oxygen-rich ambient seawater.

[39] The observed EPR abyssal hill hydrothermal mineral assemblage requires a hydrothermal fluid

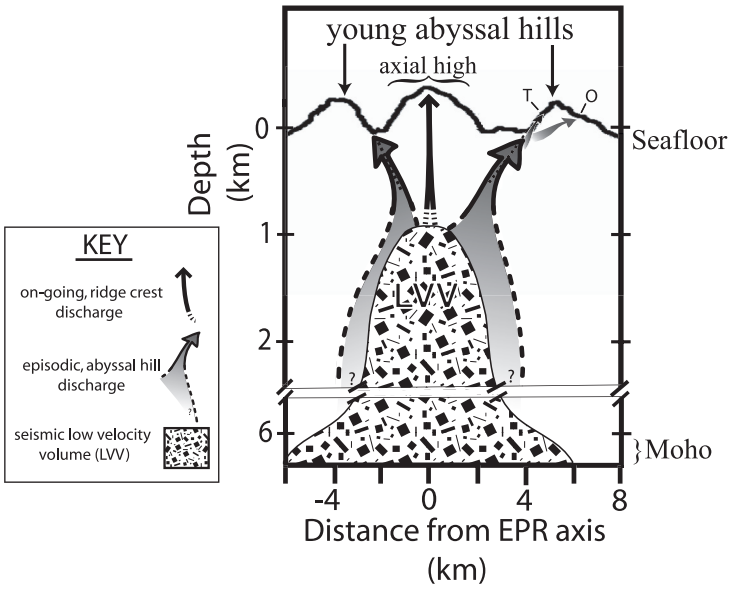

Figure 15. Schematic cross section perpendicular to the EPR axis at 10°20′N; sketch based on actual bathymetric profiles at this latitude (from *Macdonald et al.* [1992] SeaBEAM data combined with *Alvin* dive 2695 depth profile). True dips of subseafloor faults are unknown, and the dips shown (dashed lines) represent extrapolations of exposed abyssal hill fault scarps dips into the subsurface. Stippled region represents the seismic Low Velocity Volume (LVV), i.e., the melt zone beneath the EPR crest, which is shown here by scaling the *Dunn et al.* [2000] model for the LVV at EPR, 9°30′N to fit the narrower dimensions of the triangular axial high at 10°20′N. Approximate locations of Tevnia and Ochre Sites are indicated by "T" and "O," respectively. Arrows indicate paths of hydrothermal discharge. High T (>250°C) fluids discharge at ridge-axis (0 km) and lower T fluids (<150°C) discharge from young abyssal hills (∼1–5 km away from ridge axis, i.e., ∼0.1 Ma). Dashed and broadened arrow tails indicate uncertainties about flow paths and fluid source depths. We propose that fluids discharging from the axis and from adjacent, young abyssal hills both are derived from the hot margins of the axial melt zone within basaltic crust (see text).

enriched in Fe, K, Mn, and Si, and depleted in Mg. Most basalt-hosted ridge crest "end-member" hydrothermal fluids exhibit these chemical characteristics [*Von Damm*, 1995]. *Edmond et al.* [1979a, 1979b] and *Bischoff* [1980] argued that high temperature basalt-seawater reaction is needed to enrich fluids in K and metals, and basalt-seawater interaction experiments show that seawater K is removed into basalt alteration products at reaction temperatures below 70°C, and released from basalt at temperatures above 150°C [e.g., *Bischoff and Seyfried*, 1978; *Seyfried and Bischoff*, 1979; *Seyfried*, 1987; *Seyfried et al.*, 1991]. *Von Damm* [1995] has shown that enrichments in K and metals are greatest in high-chlorinity axial vent fluids that have undergone subseafloor phase separation at high temperatures. On the EPR axis at 9°–10°N, time series studies of vent fluid composition have demonstrated that when phase separation occurs, low-chlorinity condensed vapors are vented first while denser, high-chlorinity conjugate fluids remain sequestered within the seafloor [*Von Damm et al.*, 1997; *Von Damm*, 2000]. If axial fluid flow pathways are clogged by mineral precipitation before the high chlorinity fluids are pumped out, these brines could be trapped within the seafloor for an indefinite time period. Subsequent breaching of such an isolated brine reservoir by off-axis faulting could supply young abyssal hills with deep-sourced hydrothermal fluids characterized by low Mg and high concentrations of Cl, K, Si and metals. Alternatively, seawater that penetrates downward along off-axis faults to the margins of the EPR axial magma chamber could react at high temperatures to form low Mg, K-, Si- and metal-enriched hydrothermal fluids that discharge from young abyssal hills (Figure 15). In either case, conductive cooling of high temperature fluids would cause Cu and Zn sulfides to precipitate within the seafloor, resulting in both the Mg-poor, Si-, K- Fe- and Mn rich mineral composition that we observe at our EPR abyssal hill sites and in discharge temperatures <150°C. Alternatively, loss of Cu and Zn can be caused by fluid pH increase; increase in fluid pH from carbonate vein dissolution within the seafloor has been advanced to explain metal depletion in 308°C fluids discharging at the Sea Cliff vents, located 2.6 km east of the

Gorda Ridge axis on the faulted wall of the axial rift valley (K. Von Damm, personal communication, 2005).

[40] Potassium enrichment and celadonite formation in volcanic flows of Hole 504b, located on the Nazca plate south of the Costa Rica Rift, extend from the sediment/basement interface down to ~200 m above the base of the volcanic section [*Alt*, 1995]. Uptake of K from seawater into basalt at low temperature is the generally accepted cause of this enrichment, however it is possible that hydrothermal flux through abyssal hills may also contribute. The thickness of seismic layer 2A (widely assumed to be the volcanic extrusive layer) at the EPR axis is estimated to be approximately 200 m [*Christeson et al.*, 1994]. Development of off-axis faults begins 1–3 km away from the EPR axis [*Carbotte and Macdonald*, 1992], where the thickness of seismic layer 2A is 300–600 m [*Christeson et al.*, 1994]. As the volcanic pile accumulates, the most porous flows are the youngest flows at the top that have not yet been compacted and sealed by mineralization. Therefore it is conceivable that K-enrichment and celadonite formation in the uppermost 300–400 m of the volcanic section occurs by episodic injection of potassic, ferrous, conductively cooled axial hydrothermal fluids that travel upward along off-axis faults and into porous upper lava flows. This speculation is consistent with the hydrothermal origin suggested by *Alt and Teagle* [2003] for celadonite occurring in fast-spread basement drill core from ODP Site 801 in the southwestern Pacific. *Alt and Teagle* [2003] argue that the celadonite and overlying massive Si-Fe deposit found at Site 801 were formed from venting at the ridge axis. However, sediment intercalated with the volcanic flows beneath the deposit, and the low $\delta^{13}C$ values of carbonate veins in these flows compared to basalt flows deeper in the hole (indicating fluid interaction with carbonate sediments), together suggest that the Si-Fe deposit and celadonite formed off-axis on the ridge flank. The Site 801 Si-Fe deposit is 10–20 m thick. No deposit of this description has yet been found at the axis of a fast spreading ridge. We propose that thick Fe-Si-Mn deposits may be more typical products of ridge flank hydrothermal systems.

[41] Lastly, the composition of the Tevnia and Ochre Site EPR abyssal hill hydrothermal precipitates reflects mixing at the seafloor between ambient seawater and end-member hydrothermal fluids created by reaction of seawater and basalt. It is distinctively different from the calcium carbonate + brucite mineral assemblage precipitated on the seafloor from Mg-rich, alkaline fluids venting at the ultramafic-hosted Lost City hydrothermal site on the MAR flank [*Blackman et al.*, 1998; *Kelley et al.*, 2001]. It is likely that the EPR abyssal hill hydrothermal pathways at our study site do not penetrate below the Moho, and are not tapping fluids involved in serpentinization.

10. Implications for Geometry of Fluid Flow

[42] The geometry of fluid flow on ridge flanks is poorly known and much debated [*Fisher et al.*, 2003a; *Fisher and Becker*, 2000; *Fisher*, 1998; *Johnson et al.*, 1993; *Davis et al.*, 1989, 1999; *Baker et al.*, 1991, *Wheat et al.*, 2004, and references therein]. *Fehn et al.* [1983] made a distinction between "active" hydrothermal convection cells driven by heat from magmatic sources beneath the ridge crest, and migrating "passive" ridge flank convection cells driven by heat within the spreading plate. The region of transition from "active" to "passive" hydrothermal convection is not well-defined, and probably varies greatly with spreading rate. Also, recent seismic tomography along the EPR in our study area suggests that mantle melt sources (i.e., seismic low velocity zones) are not perfectly aligned beneath the EPR axial high [*Toomey et al.*, 2003]. For the global MOR, *Stein et al.* [1995] adopted the terminology "axial" for hydrothermal flux from 0–0.1 Ma lithosphere, "near-axial" for flux from 0.1–1 Ma lithosphere, and "off-axial" for flux from >1 Ma lithosphere. However, on the fast spreading EPR the term "off-axis" commonly refers to hydrothermal activity that is outside the narrow (<0.3 km) axial summit zone, but still on the 1–8 km-wide axial high; and the term "ridge flank" commonly refers to the region adjacent to the axial high, with no age limitation.

[43] For greater clarity and applicability to different hydrothermal regimes on fast spreading ridges, we use "axial" to refer to vents on the axial high, and to fluids circulating in "active" systems powered by melt sources beneath the axial high. We use "young abyssal hills" to refer to the zone adjacent to the axial high in which active faulting and uplift of hills is occurring. We suggest that "mature abyssal hills" be applied to abyssal hill terrain that is outside the zone of active faulting and hill uplift, but which is not yet buried by sediments, and that "buried abyssal hills" be applied to older ridge

flank regions where advective heat loss is still occurring beneath a continuous cover of sediment pierced only by isolated volcanic seamounts [e.g., *Fisher et al.*, 2003a, 2003b].

[44] The EPR abyssal hill site that we describe here is only ~5 km away from the ridge axis, and is adjacent to a narrow axial high. Our site is in the "young abyssal hill" zone, as defined above, and possibly at the transition between "active" and "passive" hydrothermal circulation. Figure 15 shows a schematic cross section perpendicular to the EPR axis based on the actual bathymetric depth profile at 10° 20′N. The schematic cross section depicts spatial relationships between the axial high, the youngest abyssal hills, and the axial seismic low velocity volume (LVV). In this figure we use the seismic tomography model of the LVV developed by *Dunn et al.* [2000] for the EPR at 9°30′N, and scale it down horizontally to match the relatively narrower width of the axial high at 10°20′N. Both the actual width of the LVV at 10°20′N and the actual dips and depths of the fault planes bounding the abyssal hills are unknown. Given these uncertainties, there are two possible scenarios: (1) if the dips of the inward-facing abyssal hill faults in the upper 1 km are shallow or listric, or if the LVV top is wider than the depicted width (closer to the imaged width of the LVV top at 9°30′N), then the subseafloor inward-dipping fault planes of the youngest abyssal hills extend to the region above the melt-bearing LVV beneath the axial high; (2) if the inward-dipping fault plane dips are steep, then the fault planes essentially bound the margins of the LVV model. In both scenarios, hydrothermal circulation taps heat from the LVV, and fluids at the abyssal hill sites are conductively cooled products of basalt interaction (± phase separation) from high temperature source regions proximal to the LVV.

[45] Figure 15 illustrates the possible source regions for fluids emitted at the ridge axis and from the youngest abyssal hills. The depths of abyssal hill hydrothermal fluid sources are depicted ambiguously (dashed) since these depths depend on the unknown dips and depths of the fault planes. The broadening of the LVV below the Moho proposed by *Dunn et al.* [2000] suggests that cooling of the edges of the LVV extends to the base of the crust and takes place in a very narrow region adjacent to the axial high. However, there is no independent evidence that brittle faults so close to the axial high extend to near the Moho. Furthermore, to cool the LVV margin to great depth in such a narrow zone adjacent to the axial high requires a very large hydrothermal flux from the youngest abyssal hills, a circumstance for which there also is insufficient evidence. We note that the Tevnia and Ochre Site hydrothermal mineral assemblages are identical, suggesting that the two deposits precipitated from fluids that are chemically and thermally indistinguishable despite their locations on opposing scarps bounding both sides of the hill. This most likely means that (1) fluids ascending along the western fault zone also migrated laterally through the porous upper lava flows of the hill to vent from the eastern side of the hill and/or that (2) ridge-parallel hydrothermal convection down to the brittle/ductile transition takes place along both inward- and outward-facing ridge flank faults, and mines heat from a wider zone at the LVV margin than the *Dunn et al.* [2000] model suggests. Figure 15 is different from most 2-D conceptual figures of mid-ocean ridge fluid flow that have been published because, as required by our observations, it shows faults adjacent to the axial high as fluid upflow zones rather than fluid down-flow zones. In three dimensions, we expect that ridge-parallel faults are permeable conduits for both down-flow and up-flow, and that they channel a significant component of ridge-parallel fluid flow. The extent to which these faults serve as channels for ridge-perpendicular flow is unknown.

11. Implications for Episodicity and Longevity of Fluid Flow

[46] A complicated history of brecciation, alteration, cementing, rebrecciation, and recementing is evident in the hydrothermal samples from Tevnia Site. In thin section, at least three generations of brecciation followed by hydrothermal cementation are observed. These petrographic relationships appear to record pulses of hydrothermal discharge following punctuated tectonic events. The colonies of undisturbed tube worm tubes and the live microbial mats on the western fault scarp lead us to suggest that these deposits have been continually forming over an extended period of time that included a relatively recent episode of hydrothermal venting. The inclusion of pelagic sediment throughout the matrices of the deposits further supports an extended period of formation, requiring enough time to incorporate material from the steady, slow rain of biogenic fallout through the water column.

[47] The throw on the western fault scarp is at least 200 m (more if lava flows from the ridge axis have

dammed against the base of the scarp [*Macdonald et al.*, 1996]). Since the lithosphere at this site is 100,000 years old, an average uplift rate of at least 2 mm/year is required to produce the observed throw. Earthquakes recorded on the EPR flanks are typically small (<M5), and therefore we assume that vertical displacements for each slip event on abyssal hill faults also are small, on the order of a few centimeters. If the average uplift rate is 2 mm/yr, then slip on the western fault repeats on a decadal timescale. Additionally, frequent and sometimes large (>M6) earthquakes are generated from slip along the nearby Clipperton Transform fault. *Haymon et al.* [2005] proposed that young, actively uplifting EPR abyssal hills experience frequent seismically triggered episodes of hydrothermal fluid flow, in response to hydraulic fluid pulses [*Wilcock*, 2004] and to shaking that opens mineral-clogged fluid flow paths. In this way, abyssal hill hydrothermal systems may be activated semicontinuously over tens to hundreds of thousands of years until the hills cease active uplift and spread away from the seismicity of the plate boundary zone. Our evidence for multiple hydrothermal cementation events on the fault scarp at Tevnia Site supports this proposal, as do direct observations of changes in the fluid flow rates and compositions of marine and terrestrial springs before and after earthquakes [*Johnson et al.*, 2001; *Sohn et al.*, 1998; *Wilcock*, 2004; *Claesson et al.*, 2004].

12. Summary of Observations and Conclusions

12.1. Summary of Observations

[48] On the basis of the mineral and chemical content, morphology, and petrographic relationships observed in samples of the mineral deposits at Tevnia and Ochre Sites, and the types of vent fauna observed at the sites, constraints have been placed on hydrothermal fluid composition and sources, temperatures of mineral formation, and characteristics of the depositional environment. Principal observations made in this study are as follows:

[49] 1. Petrographic observations show that the Tevnia Site mineral deposits are breccias with hydrothermal, volcanic, sedimentary, and fossil fauna components that exhibit at least three generations of cracking and cementation. The Ochre Site samples are pure hydrothermal encrustations formed on a basaltic seafloor substrate.

[50] 2. The hydrothermal component of samples from both sites is composed of: x-ray amorphous opaline silica and hydrous Fe-oxide phases, crystalline Mn-oxides (birnessite and todorokite), irregular mixed-layer Fe-smectite-mica (nontronite-celadonite), and calcite (residual from sedimentary microfossils in matrix). A distinctive mineral zonation is evident in these samples: (*bottom/interior*) mixed layer nontronite-celadonite → (*middle*) hydrous Fe-oxide and opaline silica → (*upper/exterior*) Mn-oxide. Observed textures, minerals, and microfossils in the EPR abyssal hill samples, combined with the absence of copper and zinc minerals, clearly distinguishes these samples from inactive high-temperature (>250°C) hydrothermal vent deposits found on the EPR axis.

[51] 3. Intact tubes from *Tevnia* tube worms, a vent-endemic species that colonizes active vent sites on the EPR crest, were found at both sites. Dive video shows extensive mossy microbial mats attached to the exposed volcanic substrate at both sites. Other live fauna observed or photographed include galatheid crabs, shrimp, and colonial "dandelions". Fossil fauna that are observed at the sites, or are preserved by hydrothermal minerals in thin sections, include a bivalve shell (possibly a *Calyptogena* clam), filamentous microbes, and both planktonic and benthic formaniferans.

12.2. Summary of Implications and Conclusions

[52] 1. Petrologic evidence suggests that the mineral deposits at Tevnia Site accreted on the exposed fault scarp during repeated episodes of faulting and subsequent fluid discharge as the abyssal hill was uplifted, sedimented, and moved off-axis. Presence of intact worm tubes and live microbial mats at both sites indicates that the most recent episode had waned only months before the sites were visited in 1994. We propose that young abyssal hill hydrothermal systems flow intermittently in response to frequent (decadal) seismic events repeated over time periods of 10^4–10^5 years, until the hills stop growing and move out of the active plate boundary zone.

[53] 2. Mineral assemblages and elemental compositions of the deposits reflect precipitation from K-, Si-, and metal-enriched hydrothermal fluids that likely were derived from high-temperature seawater-basalt interaction proximal to the axial melt zone. Possibly, abyssal hill faults tap residual ridge crest brines that previously have undergone: phase separation plus loss of a conjugate vapor phase;

conductive cooling to temperatures <150°C; and, loss of Cu and Zn sulfides within the seafloor prior to venting. These fluids may contribute to formation of the earliest celadonitic alterion assemblage observed in oceanic crust [*Alt*, 1995; *Alt and Teagle*, 2003].

[54] 3. If the fluid source for the Tevnia and Ochre Sites lies above the melt zone beneath the ridge crest, fluid flow perpendicular to the ridge axis is required; if the fluid source resides beneath the ridge flank alongside the melt zone, ridge parallel convection along ridge flank faults is possible. Ridge parallel convection along abyssal hill faults would facilitate heat advection and chilling along the edges of the axial melt zone within the crust, as previously proposed by others [*McClain et al.*, 1985; *Dunn et al.*, 2000].

[55] 4. Fe-Si-Mn deposits are a distinctive petrologic class of marine hydrothermal deposits that form in basalt-hosted, fault-controlled hydrothermal systems at moderate to low temperatures. This class of deposits is found on spreading ridges and ridge flanks throughout the world ocean (see Table 5), and also is common in the volcanic sections of ophiolites. Given the diversity of environments where these hydrothermal deposits have been reported, and the magnitude of estimated hydrothermal heat loss from 0.1–5 Ma abyssal hill terrain, it seems likely that young abyssal hill hydrothermal fluxes significantly impact global geochemical budgets. More exploration of abyssal hills on ridge flanks is required to estimate the geographic distribution and average chemistry of vents, and the magnitude of geochemical fluxes from abyssal hill hydrothermal systems.

[56] 5. If young abyssal hills host widespread hydrothermal systems that are seismically rejuvenated by earthquakes at frequent (decadal timescale) intervals, these systems may be important to deep-sea hydrothermal biota, allowing larva of hydrothermal vent animals to disperse across the mid-ocean ridge, as well as along the ridge crest. The microbes inhabiting the subseafloor biosphere on ridge flanks may be contiguous with the microbial biosphere on the ridge crest, and may be flushed out of abyssal hills by seismically triggered pulses of fluid flow [*Haymon et al.*, 2005]. These exciting possibilities can and should be tested by future exploration of abyssal hills.

Acknowledgments

[57] We thank Ken Macdonald and Jeff Fox for providing us with the samples, dive data/images, and dive observations that were necessary to this study. We also thank Ken Macdonald, Chris Ehrhardt, Doug Wilson, and Suzanne Carbotte for very helpful scientific discussions. Tessa Hill and Tim Shank generously assisted us with fauna identifications. We are grateful to Cris Little and Bob Embley for their thorough and constructive reviews of the original manuscript and to Cris Little for his assistance in fossil identification. This research was supported by National Science Foundation grants OCE-0002816 (to R. Haymon), OCE9816021 (to K. Macdonald), and OCE0324668 (to R. Haymon and K. Macdonald); NOAA-OE grant NA04OAR600049 (to R. Haymon and K. Macdonald); and an Office of Naval Research grant (to K. Macdonald and P. J. Fox).

References

Alexander, R. T., and K. C. Macdonald (1996), Sea Beam, SeaMARC II and ALVIN- based studies of faulting on the East Pacific Rise 9°20′N–9°50′N, *Mar. Geophys. Res.*, *18*, 557–587.

Alt, J. C. (1995), Subseafloor processes in mid-ocean ridge hydrothermal systems, in *Seafloor Hydrothermal Systems: Physical, Chemical, Biological, and Geological Interactions*, *Geophys. Monogr. Ser.*, vol. 91, edited by S. Humphris et al., pp. 85–114, AGU, Washington, D. C.

Alt, J. C., and D. A. Teagle (2003), Hydrothermal alteration of upper oceanic crust formed at a fast-spreading ridge: Mineral, chemical, and isotopic evidence from ODP Site 801, *Chem. Geol.*, *201*, 191–211.

Alt, J. C., P. Lonsdale, R. Haymon, and K. Muehlenbachs (1985), Hydrothermal sulfide and oxide deposits on seamounts near 21°N, East Pacific Rise, *Geol. Soc. Am. Bull.*, *98*, 157–168.

Anderson, R. N., M. G. Langseth, and J. G. Sclater (1977), The mechanisms of heat transfer through the floor on the Indian Ocean, *J. Geophys. Res.*, *82*, 3391–3409.

Bailey, S. W. (1982), Nomenclature for regular interstratifications, *Am. Mineral.*, *67*, 394–398.

Bailey, S. W. (Ed.) (1988), *Hydrous Phyllosillicates*, *Rev. Mineral.*, vol. 19, pp. 603–604, Mineral. Soc. of Am., Washington, D. C.

Bailey, S. W., G. W. Brindley, H. Kodama, and R. T. Martin (1979), Report of the Clay Minerals Society Nomenclature Committee for 1977 and 1978, *Clays Clay Mineral.*, *27*, 238–239.

Baker, P. A., P. M. Stout, M. Kastner, and H. Elderfield (1991), Large-scale lateral advection of seawater through oceanic crust in the central equatorial Pacific, *Earth Planet Sci. Lett.*, *105*, 522–533.

Barrett, T. J., and H. Friedrichsen (1982), Elemental and isotopic compositions of some metalliferous and pelagic sediments from the Galapagos Mounds area, DSDP Leg 70, *Chem. Geol.*, *36*, 275–298.

Batiza, R., B. R. Rosendahl, and R. L. Fisher (1977), Evolution of oceanic crust: 3. Petrology and chemistry of basalts from the East Pacific Rise and the Siquieros Transform Fault, *J. Geophys. Res.*, *82*, 265–276.

Becker, K., R. P. Von Herzen, and S. Karato (1983), Geothermal measurements from drilling of sediments near the Galapagos Spreading Center 86°W, D.S.D.P. Leg 70, *Initial Rep. Deep Sea Drill. Proj.*, *70*, 445–458.

Bischoff, J. L. (1972), A ferroan nontronite form the Red Sea geothermal system, *Clays Clay Mineral.*, *20*, 217–223.

Bischoff, J. L. (1980), Geothermal systems at 21°N, East Pacific Rise: Physical limits on geothermal fluid and role of adiabatic expansion, *Science*, *207*, 1465–1469.

Bischoff, J. L., and W. E. Seyfried (1978), Hydrothermal chemistry of seawater from 250 to 350°C, *Am. J. Sci.*, *278*, 838–860.

Blackman, D., J. Cann, B. Janesen, and D. Smith (1998), Origin of extensional core-complexes: Evidence from the Mid-Atlantic Ridge at Atlantis Fracture Zone, *J. Geophys. Res.*, *103*, 21,315–21,333.

Bohlke, J. K., J. C. Alt, and K. Muelenbachs (1984), Oxygen isotope-water relations in altered deep-sea basalts: Low-temperature mineralogical controls, *Can. J. Earth. Sci.*, *21*, 67–77.

Boyd, T. D., and S. D. Scott (2001), Microbial and hydrothermal aspects of ferric oxyhydroxides and ferrosic hydroxides: The example of Franklin Seamount, Western Woodlark Basin, Papua New Guinea, *Geochem. Trans.*, *2*(1), 45–56, doi:10.1039/b105277m.

Buatier, M., J. Honnorez, and G. Ehret (1989), Fe-smectite-glauconite transition in hydrothermal green clays from the Galapagos Spreading Center, *Clays Clay Mineral.*, *37*, 532–541.

Cann, J. R., C. K. Winter, and R. G. Pritchard (1977), A hydrothermal deposit from the floor of the Gulf of Aden, *Mineral. Mag.*, *41*, 193–199.

Carbotte, S., and K. C. Macdonald (1992), East Pacific Rise 8°–10°30′N: Evolution of ridge segments and discontinuities from SeaMarc II and three-dimensional magnetic studies, *J. Geophys. Res.*, *97*, 6959–6982.

Carlson, R. L. (1998), Seismic velocities in the uppermost oceanic crust: Age dependence and the fate of layer 2A, *J. Geophys. Res.*, *103*, 7069–7077.

Christeson, G. L., G. M. Purdy, and G. J. Fryer (1994), Seismic constraints on shallow crustal emplacement at the fast spreading East Pacific Rise, *J. Geophys. Res.*, *99*, 17,957–17,973.

Claesson, L., A. Skelton, C. Graham, C. Dietl, M. Mörth, P. Torssander, and I. Kockum (2004), Hydrogeochemical changes before and after a major earthquake, *Geology*, *32*, 641–644.

Cole, T. G., and H. F. Shaw (1983), The nature and origin of authigenic smectites in some recent marine sediments, *Clay Miner.*, *18*, 239–252.

Corliss, J. B., M. Lyle, J. Dymond, and K. Crane (1978), The chemistry of hydrothermal mounds near the Galapagos Rift, *Earth Planet Sci. Lett.*, *40*, 12–24.

Crerar, D. A., and H. L. Barnes (1976), Ore solution chemistry, Part 5, *Econ. Geol.*, *71*, 772–794.

Crowder, L. K., and K. C. Macdonald (2000), New constraints on the width of the zone of active faulting on the East Pacific Rise 8°30′N–10°00′N from Sea Beam bathymetry and SeaMARC II side-scan sonar, *Mar. Geophys. Res.*, *21*, 513–527.

Davis, E. E., D. S. Chapman, C. Forster, and H. Villinger (1989), Heat flow variations correlated with buried basement topography on the Juan de Fuca Ridge flank, *Nature*, *342*, 533–537.

Davis, E. E., D. S. Chapman, K. Wang, H. Villinger, A. T. Fisher, S. W. Robinson, J. Grigel, D. Pribnow, J. Stein, and K. Becker (1999), Regional heat flow variations across the sedimented Juan de Fuca Ridge eastern flank: Constraints on lithospheric cooling and lateral hydrothermal heat transport, *J. Geophys. Res.*, *104*, 17,675–17,688.

Decarreau, A., and D. Bonnin (1986), Synthesis and crystallogenesis at low temperature of Fe (III)-smectites by evolution of coprecipitated gels: Experiments in partially reducing conditions, *Clay Miner.*, *21*, 861–877.

Decarreau, A., D. Bonnin, D. Badaut-Trauth, R. Couty, and P. Kaiser (1987), Synthesis and cystallogenesis of ferris smectite by evolution of Si-Fe coprecipitates in oxidizing conditions, *Clay Miner.*, *22*, 207–223.

DeMets, C., R. G. Gordon, D. F. Argus, and S. Stein (1990), Current plate motions, *Geophys. J. Int.*, *101*, 425–478.

DeMets, C., R. G. Gordon, D. F. Argus, and S. Stein (1994), Effect of recent revisions to the geomagnetic reversal time scale on estimates of current plate motions, *Geophys. Res. Lett.*, *21*, 2191–2194.

Dunn, R. A., D. R. Toomey, and S. C. Solomon (2000), Three-dimensional seismic structure and physical properties of the crust and shallow mantle beneath the East Pacific Rise at 9°30′N, *J. Geophys. Res.*, *105*, 23,537–23,555.

Edmond, J. M., C. Measures, B. Mangum, B. Grant, F. R. Sclater, R. Collier, A. Hudson, L. I. Gordon, and J. B. Corliss (1979a), On the formation of metal-rich deposits at ridge crests, *Earth Planet Sci. Lett.*, *46*, 19–30.

Edmond, J. M., C. Measures, R. McDuff, L. H. Chan, R. Collier, B. Grant, L. I. Gordon, and J. B. Corliss (1979b), Ridge crest hydrothermal activity and the balances of the major and minor elements in the ocean: The Galapagos data, *Earth Planet Sci. Lett.*, *46*, 1–18.

Edwards, K. J., W. Bach, T. M. McCollom, and D. R. Rogers (2004), Neutrophilic iron-oxidizing bacteria in the ocean: Habitats, diversity, and their roles in mineral deposition, rock alteration, and biomass production in the deep-sea, *Geomicrobiol. J.*, *21*, 393–404.

Emerson, D., and C. L. Moyer (2002), Neutrophilic Fe-oxidizing bacteria are abundant at the Loihi Seamount hydrothermal vents and play a major role in Fe oxide deposition, *Appl. Environ. Microbiol.*, *68*, 3085–3093.

Fehn, U., K. E. Green, R. P. Von Herzen, and L. M. Cathles (1983), Numerical models for the hydrothermal field at the Galapagos Spreading Center, *J. Geophys. Res.*, *88*, 1033–1048.

Fisher, A. T. (1998), Permeability within basaltic oceanic crust, *Rev. Geophys.*, *36*, 143–182.

Fisher, A. T., and K. Becker (2000), Channelized fluid flow in oceanic crust reconciles heat-flow and permeability data, *Nature*, *403*, 71–72.

Fisher, A. T., et al. (2003a), Hydrothermal recharge and discharge across 50 km guided by seamounts on a young ridge flank, *Nature*, *421*, 618–621.

Fisher, A. T., C. A. Stein, R. N. Harris, K. Wang, E. A. Silver, M. Pfender, M. Hutnak, A. Cherkaoui, R. Bodzin, and H. Villinger (2003b), Abrupt thermal transition reveals hydrothermal boundary and role of seamounts within the Cocos Plate, *Geophys. Res. Lett.*, *30*(11), 1550, doi:10.1029/2002GL016766.

Fortin, D., F. G. Ferris, and S. Scott (1998), Formation of Fe-silicates and Fe oxides on bacterial surfaces in samples collected near hydrothermal vents on the Southern Explorer Ridge in the northeast Pacific Ocean, *Am. Mineral.*, *83*, 1399–1408.

Goodman, B. A., J. D. Russell, and A. R. Fraser (1976), A Mossbauer and IR spectroscopic study of the structure of nontronite, *Clays Clay Miner.*, *20*, 217–223.

Grill, E. V., R. L. Chase, R. D. Macdonald, and J. W. Murray (1981), A hydrothermal deposit from the Explorer Ridge in the northeast Pacific ocean, *Earth Planet. Sci. Lett.*, *52*, 142–150.

Harder, H. (1976), Nontronite synthesis at low temperatures, *Chem. Geol.*, *18*, 169–180.

Harder, H. (1977), Clay mineral formation under lateritic conditions, *Clay Miner.*, *12*, 281–287.

Harder, H. (1978), Synthesis of iron layer silicate minerals under natural conditions, *Clays Clay Miner.*, *26*, 65–72.

Haymon, R. M., and M. Kastner (1981), Hot spring deposits on the East Pacific Rise at 21°N: Preliminary description of mineralogy and genesis, *Earth Planet. Sci. Lett.*, *53*, 363–381.

Haymon, R. M., K. C. Macdonald, S. Benjamin, and C. J. Ehrhardt (2005), Manifestations of hydrothermal discharge from young abyssal hills on the fast-spreading East Pacific Rise flank, *Geology*, *33*, 153–156.

Hekinian, R., and Y. Fouquet (1985), Volcanism and metallogenesis of axial and off-axial structures on the East Pacific Rise near 13°N, *Econ. Geol.*, *80*, 221–249.

Hoffert, M. (1978), Hydrothermal deposits sampled by diving saucer in Transform Fault "A" near 37°N on the Mid-Atlantic Ridge, Famous area, *Oceanol. Acta*, *1*, 73–86.

Honnorez, J., et al. (1981), Hydrothermal mounds and young ocean crust of the Galapagos: Preliminary Deep Sea Drilling results, Leg 70, *Geol. Soc. Am. Bull.*, *92*, 457–472.

Honnorez, J., A. M. Karpoff, and D. Trauth-Badaut (1983), Sedimentology, mineralogy, and geochemistry of green clay samples from the Galapagos hydrothermal mounds, Holes 506, 506C, and 507D, Deep Sea Drilling Project Leg 70 (preliminary data), in *Initial Rep Deep Sea Drill. Proj.*, *70*, 211–224.

Jackson, M. L. (1969), Soil Chemical Analysis–Advanced Course, 2nd ed., Libr. of Congr. Cat., Washington, D. C.

Jambor, J. L., and J. E. Dutrizac (1998), Occurrence and constitution of natural and synthetic ferrihydrite, a widespread iron oxyhydroxide, *Chem. Rev.*, *98*, 2549–2585.

Janecky, D. R., and W. E. Seyfried (1984), Formation of massive sulfide deposits on oceanic ridge crests: Incremental reaction models for mixing between hydrothermal solutions and seawater, *Geochim. Cosmochim. Acta*, *48*, 2723–2738.

Jannasch, H. W. (1995), Microbial interactions with hydrothermal fluids, in *Seafloor Hydrothermal Systems: Physical, Chemical, Biological, and Geological Interactions*, *Geophys. Monogr. Ser.*, vol. 91, edited by S. Humphris et al., pp. 273–296, AGU, Washington, D. C.

Johnson, H. P., and M. J. Pruis (2003), Fluxes of fluid and heat from the oceanic crustal reservoir, *Earth Planet. Sci. Lett.*, *216*, 565–574.

Johnson, H. P., K. Becker, and R. Von Herzen (1993), Near-axis heat flow measurements on the northern Juan de Fuca Ridge: Implications for fluid circulation in oceanic crust, *Geophys. Res. Lett.*, *20*, 1875–1878.

Johnson, H. P., R. P. Dziak, C. R. Fisher, C. G. Fox, and M. J. Pruis (2001), Earthquakes' impact on hydrothermal systems may be far-reaching, *Eos Trans. AGU*, *82*, 233–236.

Juniper, S. K., and Y. Fouquet (1988), Filamentous iron-silica deposits from modern and ancient hydrothermal vents, *Can. Mineral.*, *26*, 859–869.

Kappel, E. S., and W. B. F. Ryan (1986), Volcanic episodicity and a non-steady state rift valley along the northeast Pacific spreading centers: Evidence from SeaMARC I, *J. Geophys. Res.*, *91*, 13,925–13,944.

Kastner, M., and J. M. Gieskes (1976), Interstitial water profiles and sites of diagenetic reactions, Leg 35, Bellingshausen abyssal plain, *Earth Planet Sci. Lett.*, *33*, 11–20.

Kelley, D., et al. (2001), An off-axis hydrothermal vent field near the Mid-Atlantic Ridge at 30N, *Nature*, *412*, 145–149.

Kennedy, C. B., S. D. Scott, and F. G. Ferris (2003), Characterization of bacteriogenic iron oxide deposits from Axial Volcano, Juan de Fuca Ridge, Northeast Pacific Ocean, *Geomicrobiol. J.*, *20*, 199–214.

Kennish, M. J., and R. A. Lutz (1999), Calcium carbonate dissolution rates on the East Pacific Rise at 21N: Results of an 8-year in-situ experiment, *Palaeogeogr. Palaeoclim. Palaeoecol.*, *154*, 293–299.

Klinkhammer, G. P., R. F. Weiss, and M. L. Bender (1977), Hydrothermal manganese in the Galapagos Rift, *Nature*, *269*, 319–320.

Klitgord, K. D., and J. D. Mudie (1974), The Galapagos Spreading Center: A near-bottom geophysical study, *Geophys. J. R. Astron. Soc.*, *38*, 563–586.

Lalou, C., E. Brichet, C. Jehanno, and H. Perez-Leclaire (1983), Hydrothermal manganese deposits from Galapagos Mounds, D.S.D.P., Leg 70, hole 509b and Alvin 3 dives 729 and 721, *Earth Planet. Sci. Lett.*, *63*, 63–75.

Little, C. T. S., S. E. Glynn, and R. A. Mills (2004), Four hundred and ninety million year record of bacteriogenic iron oxide precipitation at sea-floor hydrothermal vents, *Geomicrobiol. J.*, *21*, 415–429.

Lonsdale, P. (1977), Deep-tow observations at the mounds abyssal hydrothermal field, *Galapagos Rift, Earth Planet. Sci. Lett.*, *36*, 92–110.

Lonsdale, P., V. M. Burns, and M. Fisk (1980), Nodules of hydrothermal birnessite in the caldera of a young seamount, *J. Geol.*, *88*, 611–618.

Macdonald, K. C., et al. (1992), The East Pacific Rise and its flanks 8–18°N: History of segmentation, propagation and spreading direction based on SeaMARC II and Sea Beam studies, *Mar. Geophys. Res.*, *14*, 299–344.

Macdonald, K. C., P. J. Fox, R. T. Alexander, R. Pockalny, and P. Gente (1996), Volcanic growth faults and the origin of Pacific abyssal hills, *Nature*, *380*, 125–129.

Malahoff, A., G. M. McMurtry, J. C. Wiltshire, and H. W. Yeh (1982), Geology and chemistry of hydrothermal deposits from active submarine volcano Loihi, Hawaii, *Nature*, *298*, 234–239.

Marchig, V., U. von Stackelberg, M. Wiedicke, G. Durn, and D. Milovanovic (1999), Hydrothermal activity associated with off-axis volcanism in the Peru Basin, *Mar. Geol.*, *159*, 179–203.

Maris, C. R. P., M. L. Bender, P. N. Froelich, R. Barnes, and N. A. Luentke (1984), Chemical evidence for advection of hydrothermal solutions in the sediments of the Galapagos mounds hydrothermal field, *Geochim. Cosmochim. Acta*, *48*, 2331–2346.

McClain, J. S., J. A. Orcutt, and M. Burnett (1985), The East Pacific Rise in cross section: A seismic model, *J. Geophys. Res.*, *90*, 8627–8639.

McGregor, B. A., C. G. Harrison, J. W. Lavelle, and P. A. Rona (1977), Magnetic anomaly patterns on Mid-Atlantic Ridge crest at 26°N, *J. Geophys. Res.*, *82*, 231–238.

McMurtry, G. M., and H. Yeh (1981), Hydrothermal clay mineral formation of East Pacific Rise and Bauer basin sediments, *Chem. Geol.*, *32*, 189–205.

McMurtry, G. M., C. H. Wang, and H. W. Yeh (1983), Chemical and isotopic investigations into origin of clay minerals from the Galapagos hydrothermal mounds field, DSDP Leg 70, *Geochim. Cosmochim. Acta*, *47*, 475–489.

Moorby, S. A. (1983), The geochemistry of transitional sediments recovered from the Galapagos Hydrothermal Mounds Field during DSDP leg 70—Implications for mounds formation, *Earth Planet Sci. Lett.*, *62*, 367–376.

Morton, J. L., and N. H. Sleep (1985), A mid-ocean ridge thermal model: Constraints on the volume of axial hydrothermal heat flux, *J. Geophys. Res.*, *90*, 11,345–11,353.

Mottl, M. J., et al. (1998), Warm springs discovered on 3.5 Ma oceanic crust, eastern flank of the Juan de Fuca Ridge, *Geology*, *26*, 51–54.

Murnane, R., and D. A. Clague (1983), Nontronite from a low-temperature hydrothermal system on the Juan de Fuca Ridge, *Earth Planet Sci. Lett.*, *65*, 343–352.

Natland, J. H., et al. (1979), Galapagos hydrothermal mounds stratigraphy and chemistry revealed by deep-sea drilling, *Science*, *204*, 613–616.

Piper, D. Z., H. H. Veeh, W. G. Bertrand, and R. L. Chase (1975), An iron-rich deposit from the northeast Pacific, *Earth Planet Sci. Lett.*, *26*, 114–120.

Savin, S. M., and M. Lee (1988), Isotopic studies of phyllosilicates, in *Hydrous Phyllosilicates (Exclusive of Micas)*, *Rev. Miner.*, vol. 19, pp. 189–223, Mineral. Soc. of Am., Washington, D. C.

Seyfried, W. E. (1987), Experimental and theoretical constraints on hydrothermal alteration processes at mid-ocean ridges, *Annu. Rev. Earth Planet Sci.*, *15*, 317–335.

Seyfried, W. E., and J. L. Bischoff (1979), Low temperature basalt alteration by seawater: An experimental study at 70°C and 150°C, *Geochim. Cosmochim. Acta*, *43*, 1937–1947.

Seyfried, W. E., and K. Ding (1995), Phase equilibria in subseafloor hydrothermal systems: A review of the role of redox, temperature, pH, and dissolved on the chemistry of hot spring fluids at mid-ocean ridges, in *Seafloor Hydrothermal Systems: Physical, Chemical, Biological, and Geological Interactions*, *Geophys. Monogr. Ser.*, vol. 91, edited by S. Humphris et al., pp. 248–272, AGU, Washington, D. C.

Seyfried, W. E., W. C. Shanks, and W. E. Dibble Jr. (1978), Clay mineral formation in DSDP Leg 34 basalt, *Earth Planet Sci. Lett.*, *41*, 265–276.

Seyfried, W. E., K. Ding, and M. Berendt (1991), Phase equilibria constraints on the chenistry of hotspring fluids at mid-ocean ridges, *Geochim. Cosmochim. Acta*, *55*, 3559–3580.

Shank, T. M., D. J. Fornari, K. L. Von Damm, M. D. Lilley, R. M. Haymon, and R. A. Lutz (1998), Temporal and spatial patterns of biological community development at nascent deep-sea hydrothermal vents along the East Pacific Rise, *Deep Sea Res., Part II*, *45*, 465–515.

Shanks, W. C., J. K. Bohlke, and R. R. Seal II (1995), Stable isotopes in mid-ocean ridge hydrothermal systems: Interactions between fluids, minerals, and organisms, in *Seafloor Hydrothermal Systems: Physical, Chemical, Biological, and Geological Interactions*, *Geophys. Monogr. Ser.*, vol. 91, edited by S. Humphris et al., pp. 194–221, AGU, Washington, D. C.

Skirrow, R., and M. L. Coleman (1982), Origin of sulphur and geothermometery of hydrothermal sulphides from the Galapagos Rift, 86°W, *Nature*, *299*, 142–144.

Sohn, R. A., D. J. Fornari, K. L. V. Damm, J. A. Hildebrand, and S. C. Webb (1998), Seismic and hydrothermal evidence for a cracking event on the East Pacific Rise crest at 9°50′N, *Nature*, *396*, 159–161.

Stein, C. A., and S. Stein (1994), Constraints on hydrothermal heat flux through the oceanic lithosphere from global heat flow, *J. Geophys. Res.*, *99*(4), 3081–3095.

Stein, C. A., S. Stein, and A. Pelayo (1995), Heat flow and hydrothermal circulation, in *Seafloor Hydrothermal Systems: Physical, Chemical, Biological, and Geological Interactions*, *Geophys. Monogr. Ser.*, vol. 91, edited by S. Humphris et al., pp. 425–445, AGU, Washington, D. C.

Thompson, G., M. J. Mottl, and P. A. Rona (1985), Morphology, mineralogy and chemistry of hydrothermal deposits from the TAG area, 26°N Mid-Atlantic Ridge, *Chem. Geol.*, *49*, 243–257.

Toomey, D. R., R. A. Dunn, W. S. D. Wilcock, and R. S. Detrick (2003), Mantle structure beneath the East Pacific Rise and its relation to tectonic segmentation, axial morphology, and hydrothermal activity, *Eos Trans. AGU*, *84*(46), Fall Meet. Suppl., Abstract B12A-0743.

Von Damm, K. L. (1995), Controls on the chemistry and temporal variability of seafloor hydrothermal fluids, in *Seafloor Hydrothermal Systems: Physical, Chemical, Biological, and Geological Interactions*, *Geophys. Monogr. Ser.*, vol. 91, edited by S. Humphris et al., pp. 222–247, AGU, Washington, D. C.

Von Damm, K. L. (2000), Chemistry of hydrothermal vent fluids from 9–10°N, East Pacific Rise: Time zero, the immediate post-eruptive period, *J. Geophys. Res.*, *105*(B5), 11,203–11,222.

Von Damm, K. L., et al. (1997), Direct observation of the evolution of a seafloor 'black smoker' from vapor to brine, *Earth Planet Sci. Lett.*, *149*, 101–111.

Wheat, C. G., H. W. Jannasch, M. Kastner, J. N. Plant, E. H. DeCarlo, and G. Lebon (2004), Venting formation fluids from deep-sea boreholes in a ridge flank setting: ODP Sites 1025 and 1026, *Geochem. Geophys. Geosyst.*, *5*, Q08007, doi:10.1029/2004GC000710.

Wilcock, W. S. D. (2004), Physical response of mid-ocean ridge hydrothermal systems to local earthquakes, *Geochem. Geophys. Geosyst.*, *5*, Q11009, doi:10.1029/2004GC000701.

Williams, D. L., R. P. Von Herzen, J. G. Sclater, and R. N. Anderson (1974), The Galapagos Spreading Centre: Lithospheric cooling and hydrothermal circulation, *Geophys. J. R. Astron. Soc.*, *38*, 587–608.

Williams, D. L., K. Green, T. H. Van Andel, R. P. Von Herzen, J. R. Dymond, and K. Crane (1979), The hydrothermal mounds of the Galapagos Rift: Observations with DSRV Alvin and detailed heat flow studies, *J. Geophys. Res.*, *84*, 7467–7484.

Yee, N., V. R. Phoenix, K. O. Konhauser, L. Benning, and F. G. Ferris (2002), The effect of bacteria on Si precipitation at neutral pH: Implications for bacterial silicification in geothermal hot springs, *Chem. Geol.*, *199*, 83–90.